Influence of the Kuroshio Interannual Variability on the Summertime Precipitation over the East China Sea and Adjacent Area

BOLAN GAN

Key Laboratory of Physical Oceanography/Institute for Advanced Ocean Studies, Ocean University of China and Qingdao National Laboratory for Marine Science and Technology, Qingdao, China

YOUNG-OH KWON, TERRENCE M. JOYCE, AND KE CHEN

Department of Physical Oceanography, Woods Hole Oceanographic Institution, Woods Hole, Massachusetts

LIXIN WU

Key Laboratory of Physical Oceanography/Institute for Advanced Ocean Studies, Ocean University of China and Qingdao National Laboratory for Marine Science and Technology, Qingdao, China

(Manuscript received 20 August 2018, in final form 19 January 2019)

ABSTRACT

Much attention has been paid to the climatic impacts of changes in the Kuroshio Extension, instead of the Kuroshio in the East China Sea (ECS). This study, however, reveals the prominent influences of the lateral shift of the Kuroshio at interannual time scale in late spring [April–June (AMJ)] on the sea surface temperature (SST) and precipitation in summer around the ECS, based on high-resolution satellite observations and ERA-Interim. A persistent offshore displacement of the Kuroshio during AMJ can result in cold SST anomalies in the northern ECS and the Japan/East Sea until late summer, which correspondingly causes anomalous cooling of the lower troposphere. Consequently, the anomalous cold SST in the northern ECS acts as a key driver to robustly enhance the precipitation from the Yangtze River delta to Kyushu in early summer (May–August) and over the central ECS in late summer (July–September). In view of the moisture budget analysis, two different physical processes modulated by the lateral shift of the Kuroshio are identified to account for the distinct responses of precipitation in early and late summer, respectively. First, the anomalous cold SST in the northern ECS induced by the Kuroshio offshore shift is likely conducive to the earlier arrival of the mei-yu–baiu front at 30°–32°N and its subsequent slower northward movement, which may prolong the local rainy season, leading to the increased rain belt in early summer. Second, the persistent cold SST anomalies in late summer strengthen the near-surface baroclinicity and the associated strong atmospheric fronts embedded in the extratropical cyclones over the central ECS, which in turn enhances the local rainfall.

1. Introduction

As the strong western boundary current of the North Pacific subtropical gyre, the Kuroshio emerges as the poleward branch of the bifurcation of the North Equatorial Current off the Philippine coast. It flows northward past the Luzon Strait, and enters the East China Sea (ECS) through the East Taiwan Strait. Before leaving through the Tokara Strait south of Kyushu Island, the main stream of the Kuroshio primarily flows just seaward of the ECS shelf break, approximately along the 200-m isobath (Ichikawa and Beardsley 2002; Liu and Gan 2012; see Figs. 1a,b). North of about 28°N, part of the main stream diverts to the west due to the block of the Kyushu coastal topography, becoming a major source of the Tsushima Warm Current (Hsueh 2000; Guo et al. 2006), and the remainder flows along the south coast of Japan. At about 35°N, the Kuroshio leaves the coast and becomes a free jet, namely the Kuroshio Extension.

Denotes content that is immediately available upon publication as open access.

Supplemental information related to this paper is available at the Journals Online website: https://doi.org/10.1175/JCLI-D-18-0538.s1.

Corresponding author: Bolan Gan, gbl0203@ouc.edu.cn

DOI: 10.1175/JCLI-D-18-0538.1

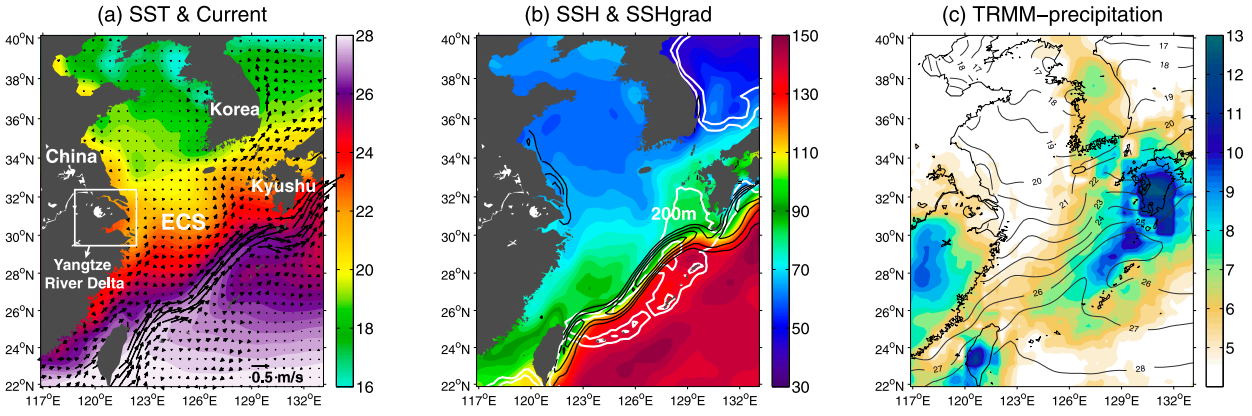

FIG. 1. Climatological May–July mean fields. (a) SST (°C; colors) and surface geostrophic velocity ($m\,s^{-1}$). (b) SSH (cm; colors) and SSH gradient [25–55 cm $(100\,km)^{-1}$; black contours with interval of 10 cm $(100\,km)^{-1}$], along with 200- and 1000-m isobaths (white contours). (c) Precipitation ($mm\,day^{-1}$; colors) with SST (°C; contours) superimposed. The SST, SSH, and surface geostrophic velocity are derived from OISST and AVISO daily data for 1994–2015, and precipitation is taken from TRMM 3B42 daily product for 1998–2015.

The Kuroshio transports a huge amount of heat from the tropics to the midlatitudes, which is largely released into the atmosphere through the intense turbulent heat flux in the Kuroshio Extension region. Thus, the Kuroshio, together with the Kuroshio Extension region, is recognized as one of the global midlatitude regions where the ocean–atmosphere interactions are most active (Kelly et al. 2010; Kwon et al. 2010). Over the past two decades, the Kuroshio Extension region, along with the Oyashio Extension region, has attracted great attention with regard to the local and remote atmospheric responses to oceanic variations in the cold season particularly, although to what extent such feedback of ocean to atmosphere contributes to the existence of the Pacific decadal oscillation remains poorly understood (Newman et al. 2016). Nevertheless, a growing body of evidence indicates that sea surface temperature (SST) variations in the Kuroshio–Oyashio Extension region during the cold season substantially affect the marine atmospheric boundary layer structure (Tokinaga et al. 2009; Masunaga et al. 2016), synoptic-scale transient eddies migrating along the North Pacific storm tracks (e.g., Nakamura et al. 2004; Gan and Wu 2013; Kwon and Joyce 2013; Small et al. 2014; Kuwano-Yoshida and Minobe 2017), blocking frequency in the eastern North Pacific (O'Reilly and Czaja 2015), basin-scale atmosphere circulation (e.g., Frankignoul et al. 2011; Taguchi et al. 2012; Gan and Wu 2012), and winter rainfall along the U.S. North Pacific coast (Ma et al. 2015). In particular, it has been pointed out that the meridional shift in the path of the Kuroshio Extension (Frankignoul et al. 2011; Kwon and Joyce 2013; Révelard et al. 2016) and the oceanic mesoscale eddies (Ma et al. 2015) leave their imprints on SST or its meridional gradient and in turn affect the wintertime atmosphere.

As noted above, extensive studies have concentrated on the wintertime atmosphere in response to oceanic changes in the Kuroshio Extension region, since the summertime atmospheric response is generally weak (e.g., O'Reilly and Czaja 2015). In comparison, fewer studies have focused on the climatic effects of the Kuroshio main stream. However, it has been revealed that the Kuroshio in the ECS can have salient impact on the mean states of local atmosphere during the warm season (e.g., Xu et al. 2011; Sasaki et al. 2012; Kunoki et al. 2015; Liu et al. 2016; Xu et al. 2018). In terms of the summertime climatological conditions in the ECS–Kuroshio region, the Kuroshio accompanies a warm-tongue SST signature of 26°–28°C (Fig. 1a), which is about 1°–2°C warmer than the adjacent continental shelf water and thus creates a strong SST front on the northwestern flank of the warm tongue. On the other hand, a large rain belt, reaching a magnitude of $12\,mm\,day^{-1}$, is nearly collocated with the Kuroshio warm tongue (Fig. 1c), indicating a potential influence of the Kuroshio on the locally enhanced rainfall. Xu et al. (2011) demonstrated a deep atmospheric response to the Kuroshio in spring (March–May), characterized by enhanced convective precipitation, frequent occurrence of cumulous convection, and surface wind convergence. Sasaki et al. (2012) further found that the warm Kuroshio anchors the overlying rain belt in early summer (June) by enhanced energetic evaporation and surface wind convergence via the pressure adjustment mechanism (Lindzen and Nigam 1987). Particularly, they concluded that the deep atmospheric response to the Kuroshio warm tongue is strongest in June, with ascent motion and diabatic heating penetrating into the upper troposphere due to deep convection. It resembles the deep-heating mode, that is, the atmospheric response

to the upstream Gulf Stream in summer reported by Minobe et al. (2010).

The locally enhanced rain belt by the Kuroshio warm tongue is embedded in the large-scale rainband that extends from southeast China to Japan (cf. Fig. 1c). This so-called mei-yu–baiu rainband (called the mei-yu in China and the baiu in Japan; e.g., Tao and Chen 1987; Ninomiya and Murakami 1987) brings the major rainy season (mid-May–mid-July) to these densely populated regions. The mei-yu–baiu rainband is strongly regulated by the East Asian summer monsoon (EASM) system, and has been widely studied in terms of seasonal progression and variability over interannual to decadal time scales (Wang and LinHo 2002; Ding and Chan 2005; Kwon et al. 2005; Ninomiya and Shibagaki 2007; Sampe and Xie 2010; Tomita et al. 2011, Xu et al. 2018, and references therein). The mean seasonal progression and variability of the mei-yu–baiu rainband have been linked primarily to the variation of summer monsoon, which is connected remotely to the tropical Indo-Pacific region (e.g., Huang et al. 2004; Ding and Chan 2005; Xie et al. 2009). In addition, we may expect a local modulation of the mei-yu–baiu rainband by the Kuroshio variability, in light of the impacts of the Kuroshio warm tongue on the atmospheric mean states (as mentioned above). However, such modulation has not yet been explored.

Unlike the mean state, the role of oceanic interannual variability in the ECS–Kuroshio region in atmospheric variability has begun to be investigated recently. Sasaki and Yamada (2018) show that the SST front variability in the ECS in June has an influence on the local precipitation in the same month, such that the strong SST front is accompanied with the heavy precipitation over the central ECS. The strong SST front mainly results from the cold SST anomalies over the continental shelf, however, for which the physical driving processes are unclear. From the perspective of ocean dynamics, an interesting question arises as to whether any variation of the Kuroshio itself would impact the summertime rainfall over the ECS and its adjacent land area, since the Kuroshio indeed exhibits a pronounced interannual variability (e.g., Wei et al. 2013). In the present study, we attempt to detect the significant response of the summertime precipitation to the Kuroshio interannual variability based on a set of high-resolution satellite observations and ERA-Interim.

The rest of the paper is organized as follows. Section 2 briefly describes the datasets and statistical methods, including the moisture budget diagnosis and the lagged maximum covariance analysis (MCA). Section 3 presents the interannual variability of the Kuroshio and its impacts on the marginal seas as well as the summertime precipitation. Section 4 investigates the possible driving mechanisms for the precipitation response. Section 5 gives a summary and discussion.

2. Data and methods

a. Satellite observations and ERA-Interim

The interannual variability of the Kuroshio is investigated based on the globally gridded sea surface height (SSH) product, which merges all SSH measurements from all satellite altimeter missions and is available daily on a 0.25° spatial resolution from January 1993 (Ducet et al. 2000), distributed by the Copernicus Marine Service, currently. The derived absolute geostrophic velocity provided by this product is also used to represent the surface geostrophic current in Fig. 1a. The daily 0.25° gridded SST data are taken from the Optimum Interpolation SST (OISST) dataset, produced by the National Oceanic and Atmospheric Administration (NOAA) (Reynolds et al. 2007). Here we used the Advanced Very High Resolution Radiometer (AVHRR)-only OISST product that combines the in situ data and the AVHRR infrared satellite SST data, available from September 1981 to the present.

To evaluate the influence of the Kuroshio interannual variability on the surface precipitation rate, we mainly used two products, the high-resolution Tropical Rainfall Measuring Mission (TRMM) Multisatellite Precipitation Analysis research-grade product (the 3B42 product; Huffman et al. 2007) and the ERA-Interim global atmospheric dataset (Dee et al. 2011). The TRMM 3B42 product has a daily 0.25° resolution with a spatial coverage of 50°N–50°S from January 1998 onward. The ERA-Interim dataset has a global grid spacing of 0.75° with 37 vertical pressure levels from January 1979 onward. Note that in general, as a high-resolution precipitation product, the TRMM product does not have the same homogeneity goals as a climate dataset like the Global Precipitation Climatology Project (GPCP). Nevertheless, we examined the GPCP daily precipitation (available on a global $1° \times 1°$ grid from October 1996 to October 2015), which shows a precipitation response pattern very similar to those based on the TRMM and the ERA-Interim datasets. However, we found that the precipitation response pattern based on the National Centers for Environmental Prediction (NCEP) Climate Forecast System Reanalysis (CFSR) product bears little resemblance to any of those derived from the above three datasets (comparing Figs. 7 and 8 and Figs. S1 and S2 in the online supplemental material). Therefore, we chose the 6-hourly fields of ERA-Interim to diagnose the moisture budget, rather than the NCEP-CFSR that was used by

Sasaki and Yamada (2018) and Xu et al. (2018). In the present study, all results are presented for the period of 1994–2015, except the TRMM precipitation product for 1998–2015.

b. Moisture budget

Following Seager and Henderson (2013) and Zhang et al. (2013), the column-integrated moisture budget equation can be written as

$$\frac{\partial\langle q\rangle}{\partial t} = -\langle\nabla\cdot(\mathbf{V}q)\rangle + S + (E-P), \tag{1}$$

where $\langle\cdot\rangle = 1/g\int_{100\text{hPa}}^{1000\text{hPa}}(\cdot)\,dp$ denotes the column-integrated quantity, $S = -(1/g)(q_s\mathbf{V}_s\cdot\nabla p_s)$ indicates the surface boundary term (the subscript s refers to surface quantities), q is specific humidity, $\mathbf{V}$ is the horizontal wind vector, p is pressure, E is evaporation, and P is precipitation. The magnitude of the S term is found to be much smaller than the others and thus can be ignored. For the seasonal and longer time scales, the local tendency term on the left-hand side of Eq. (1) is negligible. In addition, the total lateral moisture flux can be broken down into the mean-flow moisture flux and transient eddy moisture flux. Therefore, Eq. (1) can be expressed in the form of

$$\underbrace{\overline{P}-\overline{E}}_{\text{PmE}} \approx \underbrace{-\langle\nabla\cdot(\overline{\mathbf{V}}\,\overline{q})\rangle}_{\text{ConQ}^{\text{total}}} = \underbrace{-\langle\nabla\cdot(\overline{\mathbf{V}}\,\overline{q})\rangle}_{\text{ConQ}^{\text{mean}}} \underbrace{-\langle\nabla\cdot(\overline{\mathbf{V}'q'})\rangle}_{\text{ConQ}^{\text{eddy}}}, \tag{2}$$

where overbars denote the monthly mean and primes denote the submonthly disturbance. Furthermore, the monthly mean moisture flux convergence ($\text{ConQ}^{\text{mean}}$) can be decomposed into a part related to the moisture convergence by divergent mean flow (i.e., the mass convergence; $\text{ConQ}^{\text{mean}}_{\text{Div}}$) and a part related to the mean-flow advection of moisture (i.e., the advection of humidity gradient; $\text{ConQ}^{\text{mean}}_{\text{Adv}}$): namely,

$$\text{ConQ}^{\text{mean}} = \underbrace{-\langle\overline{q}\nabla\cdot\overline{\mathbf{V}}\rangle}_{\text{ConQ}^{\text{mean}}_{\text{Div}}} \underbrace{-\langle\overline{\mathbf{V}}\cdot\nabla\overline{q}\rangle}_{\text{ConQ}^{\text{mean}}_{\text{Adv}}}. \tag{3}$$

These monthly mean terms are further decomposed into the long-term monthly climatology and interannual anomalies, as $\overline{(\cdot)} = \overline{(\cdot)}_c + \overline{(\cdot)}_a$ where $\overline{(\cdot)}_c$ indicates the long-term monthly climatology and $\overline{(\cdot)}_a$ indicates the monthly deviation from the long-term monthly climatology. The anomaly form of Eq. (3) can be approximated as

$$(\text{ConQ}^{\text{mean}}_{\text{Div}})_a + (\text{ConQ}^{\text{mean}}_{\text{Adv}})_a \approx \underbrace{-\langle\overline{q}_c\nabla\cdot\overline{\mathbf{V}}_a\rangle}_{\text{ConQ}^{\text{mean}}_{\text{Div}}-\text{DYN}} \underbrace{-\langle\overline{q}_a\nabla\cdot\overline{\mathbf{V}}_c\rangle}_{\text{ConQ}^{\text{mean}}_{\text{Div}}-\text{THM}} \underbrace{-\langle\overline{\mathbf{V}}_a\cdot\nabla\overline{q}_c\rangle}_{\text{ConQ}^{\text{mean}}_{\text{Adv}}-\text{DYN}} \underbrace{-\langle\overline{\mathbf{V}}_c\cdot\nabla\overline{q}_a\rangle}_{\text{ConQ}^{\text{mean}}_{\text{Adv}}-\text{THM}}. \tag{4}$$

In Eq. (4), the dynamical and thermodynamical contributions refer to the terms only involving $\overline{\mathbf{V}}_a$ and $\overline{q}_a$, respectively. We neglected the term involving the product of $\overline{\mathbf{V}}_a$ and $\overline{q}_a$, because of its small magnitude.

c. Statistical tools

To quantify influences of the Kuroshio on the marginal seas, we conduct the lagged maximum covariance analysis (MCA), which has been widely used in the previous studies regarding the midlatitude ocean–atmosphere interaction (e.g., Czaja and Frankignoul 1999, 2002; Gan and Wu 2013, 2015; Zhang et al. 2018). The MCA isolates pairs of spatial patterns that maximize their covariance and the associated time coefficients by performing a singular value decomposition of the covariance matrix between two fields. Here the covariance matrix is constructed by the normalized SSH gradient and SST anomalies that are weighted by the cosine of latitude. The statistical significance of the MCA metrics [i.e., squared covariance (SC), squared covariance fraction (SCF), and correlation coefficient (CO) between MCA time coefficients] are based on the Monte Carlo test. Specifically, using the original SSH gradient and the SST anomalies with the time series randomly permuted, we repeated the MCA for 100 times and then obtained 100 sets of metrics, whose probability distribution function is constructed to rank the confidence level of the actual statistic. Likewise, the Monte Carlo test is also used for the statistical significance of composite analysis in section 4, for which the time domain of the composited variable is randomly scrambled by 1000 times. The influence of ocean current change is evaluated by the linear regressions onto the normalized MCA time coefficients of the SSH gradient, with the Student's t test applied. Monthly anomalies are obtained by subtracting the climatological monthly means and removing the linear long-term trend, and then three consecutive monthly anomalies are used to calculate the seasonal-mean anomalies.

3. Results

Considering that atmosphere only feels the SST change and precipitation is the ultimate product of

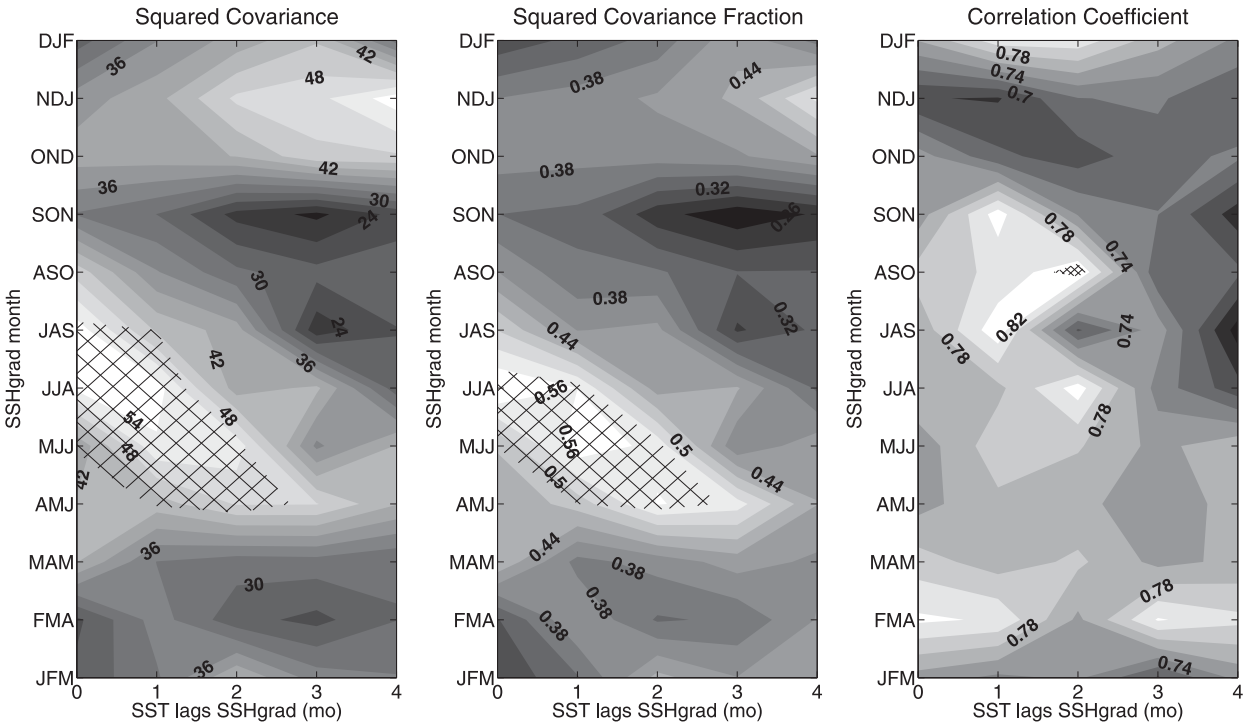

FIG. 2. (a) Squared covariance ($\times 10^3$; dimensionless), (b) squared covariance fraction, and (c) correlation coefficient of the first MCA mode between the seasonal-mean anomalies of the SSH gradient (24.625°–31.625°N, 118.125°–130.875°E) and SST (20.125°–40.125°N, 115.125°–135.125°E). The ordinate denotes the calendar months assigned to the SSH gradient for each seasonal mean, and the abscissa denotes the time lag in month for SST lagging SSH gradient (i.e., lag 1 at the JFM indicates the MCA between the JFM SSH gradient and FMA SST). Hatching areas indicate statistical significance at the 95% confidence level based on the Monte Carlo test.

ocean–atmosphere interaction, we first applied the lagged MCA to the seasonal-mean anomalies of SSH gradient and SST throughout the year to identify the most significant SST variations induced by the Kuroshio interannual variability. Note that the lagged MCA is calculated with the SSH gradient leading the SST by different time lag in months to infer an impact of the Kuroshio variability on the SST anomalies. Then we investigated the response of precipitation over the ECS and its adjacent land area through a linear regression analysis.

a. Interannual variability of the Kuroshio and its impact on the marginal seas

Figure 2 summarizes the MCA metrics for the leading MCA (hereinafter MCA1) modes between the SSH gradient anomalies fixed in one specific season and the SST anomalies lagged by 0–4 months. The seasonal-mean anomalies of the SSH gradient are used from January–March (JFM) to December–February (DJF) (moving by 1 month each time). The MCA domains for the SSH gradient and SST are set to 24.625°–31.625°N, 118.125°–130.875°E and 20.125°–40.125°N, 115.125°–135.125°E, respectively.

As can be seen from Figs. 2a and 2b, there is a coherent feature for the SC and SCF, which measures the strength of relationship between two fields in each mode and the relative importance of each mode in a given expansion, respectively. Both the SC and SCF display high significance for the relationships between the SSH gradient anomalies in April–June (AMJ) and the SST variations in the following May–July (MJJ) to July–September (JAS) (see lags 1–3). Those significant relationships are also traced in the leading modes based on the SSH gradient anomalies in MJJ [June–August (JJA)] and the SST anomalies in the following MJJ–JAS (JJA and JAS), suggesting the persistent change of the geostrophic current. Both the SC and SCF peak at JJA for the simultaneous covariability of the SSH gradient and SST. But the structure of the correlation coefficients between two MCA1 time coefficients for each lag (Fig. 2c) does not match with those of the SC and SCF, and it is barely significant at the 95% confidence level. This may be due to the small sample size (i.e., 22-yr length of each time coefficient). Nevertheless, the following analyses lend further credence to the dynamical significance of the impacts of the Kuroshio variation on SST and precipitation.

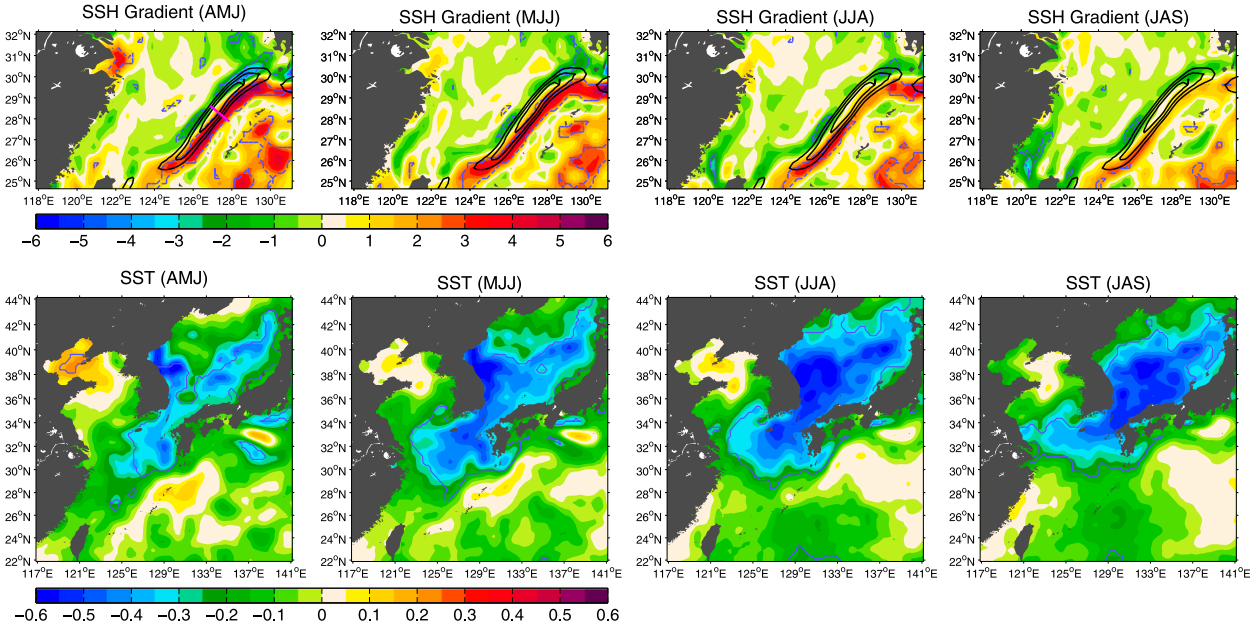

FIG. 3. Simultaneous and lagged regressions of the seasonal-mean (top) SSH gradient anomalies [cm $(100\,\text{km})^{-1}$] and (bottom) SST anomalies (°C) from AMJ to JAS against the AMJ-SSHG-MCA1 (Fig. 5a). Black contours in the top panels denote the AMJ SSH gradient climatology of 35, 45, and 55 cm $(100\,\text{km})^{-1}$, to indicate the main axis of the Kuroshio. Blue contours in each panel denote regressions significant at the 95% confidence level. Heavy magenta line in the top-left panel indicates the position of the PN line.

We analyzed the change of the Kuroshio and its impacts on the SST and atmosphere in the adjacent marginal seas based on the linear regression against the SSH gradient time coefficients of the MCA1 between AMJ SSH gradient and JJA SST (i.e., at lag 2). Particularly, we found that the time coefficients of this MCA1 mode have high correlations with the leading principal components (PC1) of the anomalous AMJ SSH gradient and JJA SST fields ($r = 0.89$ for the SSH gradient and $r = 0.96$ for SST), indicating that the dominant variations of both the geostrophic current and SST are captured by the MCA1 mode (see Fig. 3 for the corresponding spatial patterns). The PC1 explains 26.6% and 36.8% of total variance of the AMJ SSH gradient and JJA SST fields, respectively. Furthermore, the AMJ SSH gradient time coefficients are highly correlated with the corresponding time coefficients in MJJ and JJA (correlations among them reaching above 0.77). Therefore, the following results based on the AMJ SSH gradient MCA1 time coefficients at lag 2 (hereafter AMJ-SSHG-MCA1) are representative of changes related to the Kuroshio variation.

Figure 3 shows the evolution of spatial patterns of the SSH gradient and SST from AMJ to JAS associated with the AMJ SSH gradient time coefficients. The SSH gradient anomalies exhibit a persistent pattern over the 4 months with a meridional dipole whose node coincides with its climatological peak (i.e., the main axis of the Kuroshio), with the large positive anomalies appearing on the seaward flank. This dipolar pattern reflects the offshore shift of the Kuroshio on interannual time scale, as the power spectra of the AMJ-SSHG-MCA1 has a significant spectral peak at 3–4 years (not shown). The SSH gradient regression patterns suggest that the offshore state of the Kuroshio in late spring (AMJ) can persist into summer (JJA). Correspondingly, the SST regressions show that when the Kuroshio shifts offshore in AMJ, the significant cold SST anomalies emerge in the northern ECS and the Japan/East Sea in AMJ and then gradually amplify and expand northward through MJJ and JJA. Accompanied with the offshore shift of the Kuroshio in AMJ, the warm SST anomalies also emerge along the seaward of the ECS shelf break. But they are much weaker than the cold SST anomalies over the continental shelf, indicating little change of the Kuroshio warm tongue. In JAS, the cold SST anomalies are somewhat reduced in the northern ECS but retained in the Japan/East Sea.

The evolution of significant cold SST anomalies in the marginal seas is accompanied by large downward turbulent heat flux anomalies (Fig. 4, top row), as well as significant upward radiative heat flux anomalies (dominated by the shortwave radiation anomalies) that shows up over part of the northern ECS (Fig. 4, middle row). However, Fig. 4 (bottom row) shows the downward net heat flux anomalies over most parts of the marginal seas, indicating that significant cold SST anomalies are damped by gaining heat from atmosphere and thus act to impose an

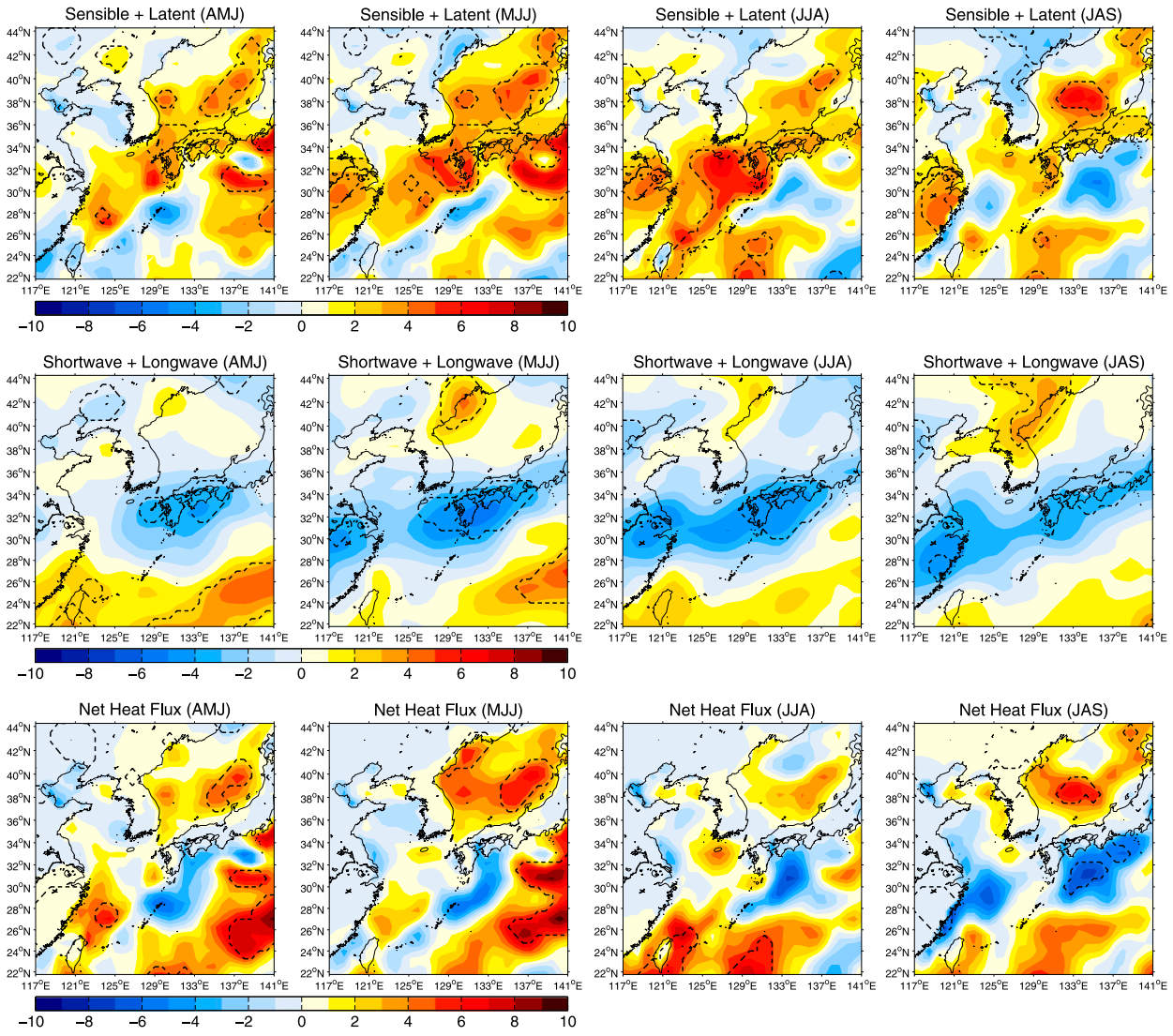

FIG. 4. As in Fig. 3, but for the regressions of (top) turbulent heat flux, (middle) radiative heat flux, and (bottom) net heat flux anomalies ($W\,m^{-2}$; positive is downward). Black dashed contours denote regressions significant at the 95% confidence level.

anomalous cooling in the lower troposphere. In fact, the significant negative radiative heat flux anomalies during AMJ–JJA coincide with the local above-normal rainfall response (see section 3b), which may imply a local thermodynamic positive feedback that the enhanced rainfall and cloudiness could amplify the preexistent cold SST anomalies by blocking the solar radiation.

Overall, the results above suggest that the persistent offshore shift of the Kuroshio since late spring primarily result in the cold SST anomalies in the marginal seas until late summer, which correspondingly causes anomalous cooling of the lower troposphere. We further constructed a simple index, the SSH slope index (SSI) at the PN line, to independently verify the persistence of the lateral shift of the Kuroshio. The SSI is defined as the absolute dynamic height difference between the two end points along the PN line (Andres et al. 2011), that is, the offshore point at 27.875°N, 127.875°E minus the onshore point at 28.625°N, 126.875°E. These two end points straddle the main axis of the Kuroshio (cf. Fig. 3, top left, magenta line), such that the SSI depicts the offshore–onshore shifts of the Kuroshio (Fig. S3). It is found that the AMJ-mean SSI significantly correlates to the AMJ-SSHG-MCA1, with a correlation coefficient of 0.75 (Fig. 5a). Furthermore, the autocorrelation coefficients of the seasonal-mean SSI throughout the year (Fig. 5b) elucidate that the Kuroshio path shift in AMJ correlates to its previous change in February–April (FMA) and persists into JJA, while the Kuroshio variation in MJJ/JJA seems to be less persistent than the case in AMJ. It is

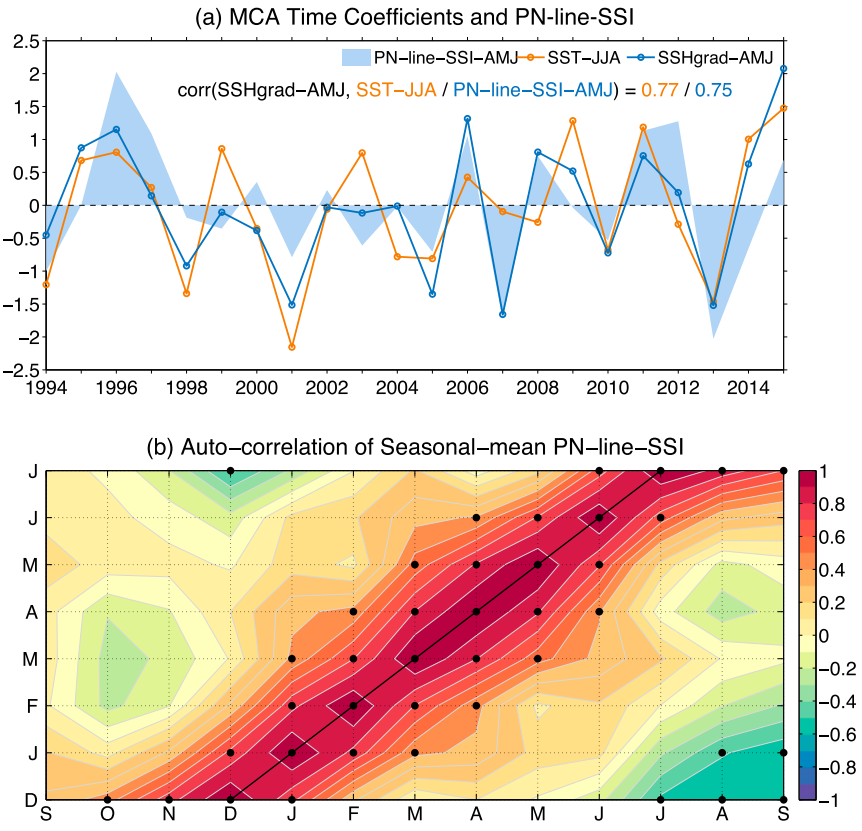

FIG. 5. (a) Normalized time coefficients of SSH gradient in AMJ (blue curve; i.e., AMJ-SSHG-MCA1) and SST in the following JJA (orange curve) derived from the corresponding MCA1 at lag 2, along with the AMJ-mean SSH slope index (SSI) at the PN line (blue shading). See section 3a for the definition of SSI. (b) Autocorrelation coefficients of the seasonal-mean SSI are plotted as a function of the calendar months (i.e., letter A denotes the AMJ mean). The black dots signify the correlations significant at the 95% confidence level.

suggested that the significant persistence of the Kuroshio shift in AMJ is a prerequisite for the covariability with SST in the marginal seas that can be significantly detected in JJA by the lagged MCA.

The offshore shift of the Kuroshio is presumed to result in the reduced onshore intrusion of warm water, which in turn induces the cold SST anomalies on the continental shelf. Indeed, comparison of the lagged regression of surface geostrophic velocity with its climatology in JJA (Fig. 6) clearly shows that the Kuroshio shifts away from the shelf break. Correspondingly, the Tsushima Warm Current and the East Korea Warm Current are significantly weakened, as implied from the anomalous southward currents to south of Cheju Island and east of South Korea. As a consequence, the anomalous cold advection likely drives the cold SST anomalies.

b. *Response of the summertime precipitation*

What is the impact of lateral shift of the Kuroshio on the precipitation over the ECS and its adjacent land area? Figure 7 displays the regression patterns of TRMM precipitation (1998–2015) from AMJ to JAS against the AMJ-SSHG-MCA1. The precipitation response exhibits two distinct patterns, one showing a zonal belt of significant positive anomalies extending from the Yangtze River delta to Kyushu during AMJ–JJA and the other showing a patch of significant positive anomalies over the central ECS in JAS. This fact indicates that the offshore shift of the Kuroshio tends to enhance the terrestrial rainfall over the Yangtze River delta and Kyushu in early summer and rainfall over the central ECS in late summer. More specifically, the strongest response of the zonal rainband occurs in MJJ (Fig. 7b), and the increased rainfall over Kyushu slightly amplifies in JJA, which is consistent with the amplification of the cold SST anomalies in the northern ECS (Fig. 3). The corresponding coefficients of determination R^2 suggest that the interannual variability of the Kuroshio lateral shift in AMJ can explain about 40% and 35% of total variance of precipitation over the Yangtze River

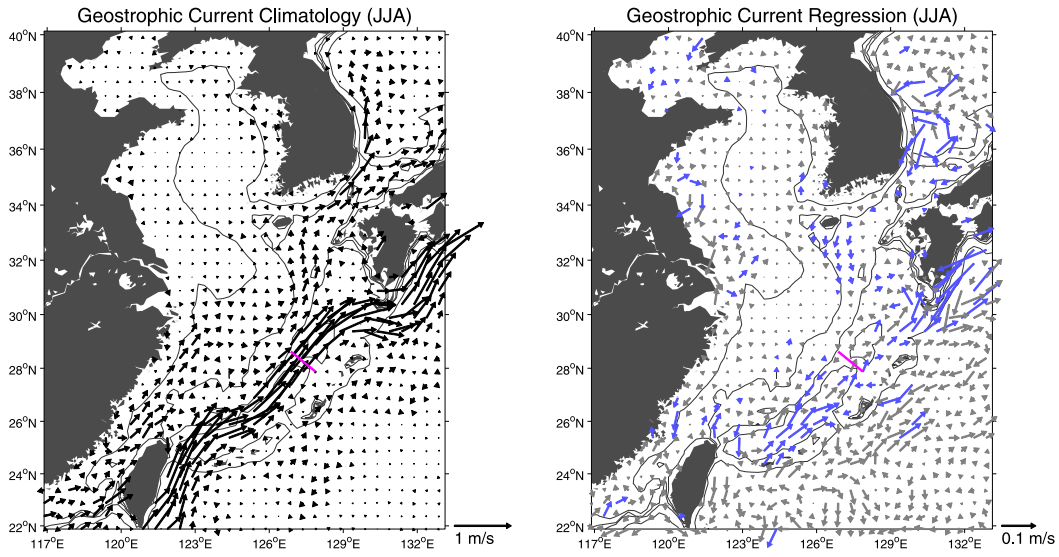

FIG. 6. (left) Climatology of surface geostrophic velocity in JJA and (right) its lagged regression on the AMJ-SSHG-MCA1, along with 50-, 100-, 200-, and 1000-m isobaths (contours). Blue vectors denote regressions significant at the 95% confidence level. Note that the mean Kuroshio mainly flows along the 200-m isobath (i.e., the shore side of the regular PN line section signified by the heavy magenta line) before leaving through the Tokara Strait. For a better visualization, the regression coefficients are magnified to 6 times the climatology scale.

delta in MJJ (Fig. 7f) and over Kyushu in JJA (Fig. 7g), respectively.

The regression patterns of total precipitation (the sum of large-scale precipitation and convective precipitation) based on the ERA-Interim product (1994–2015) bear great resemblance to the TRMM-observation-based patterns, albeit with smaller magnitude of anomalies for the former (comparing Fig. 8 with Fig. 7). It is also clearly shown that the precipitation response is dominated by the large-scale precipitation rather than the convective precipitation (Fig. 8). Since the resolution of SST data prescribed at the lower boundary of ERA-Interim has been improved from 1.0° to 0.5° after January 2002, we further examined the regressions of precipitation in 2002–15 and found that the spatial patterns are nearly identical to those since 1994 (comparing Fig. S4 with Fig. 8). The regression magnitudes since 2002, however, are generally 30%–70% higher than before and closer to those of the TRMM-observation-based results. It could imply that the simulation of atmospheric structure might be improved by resolving finer oceanic states, as suggested by Masunaga et al. (2015). In addition to the above-normal rainband, the rainfall seems to be suppressed over the northern half of the domain, but the significant decreased signals are weaker than the increased signals and its acting area changes among different precipitation products. Therefore, next, we performed an independent regression analysis to validate the robustness of the precipitation response.

Recalling that the significant cold SST anomalies and the prominent downward turbulent heat flux anomalies over the northern ECS are closely related to the offshore shift of the Kuroshio (Fig. 4), it is expected that the SST interannual variation in the northern ECS is a key driver for the precipitation response over the surrounding area. Given that, we constructed the time series of SST anomalies area-averaged in the northern ECS (30.125°–34.125°N, 124.625°–130.125°E; see box in Fig. 9b) in MJJ, which is found to be well correlated with the PC1 of MJJ SST in the entire ECS (24.125°–36.125°N, 120.125°–131.125°E; $r = 0.88$) that explains about 50.6% of the total MJJ SST variance. As expected, the corresponding SST spatial pattern in MJJ shows a monopole cold anomaly over the continental shelf (very similar to the EOF1 pattern), which is associated with the offshore shift of the Kuroshio in the previous AMJ (see Figs. 9a,b). Particularly, further inspection finds that the SSH gradient regressions are largest in AMJ rather than MJJ, suggesting that the SST response to the Kuroshio change may need at least one month to be fully developed. The cold SST anomalies in MJJ are quite persistent into JAS, which are clearly associated with the significant downward net heat flux (Figs. 9c,d), but the local sea level pressure (SLP) does not change significantly (not shown). Thus, it supports the fact that the cold SST anomalies in the northern ECS are likely to be generated by the offshore shift of the Kuroshio rather than the local atmospheric processes.

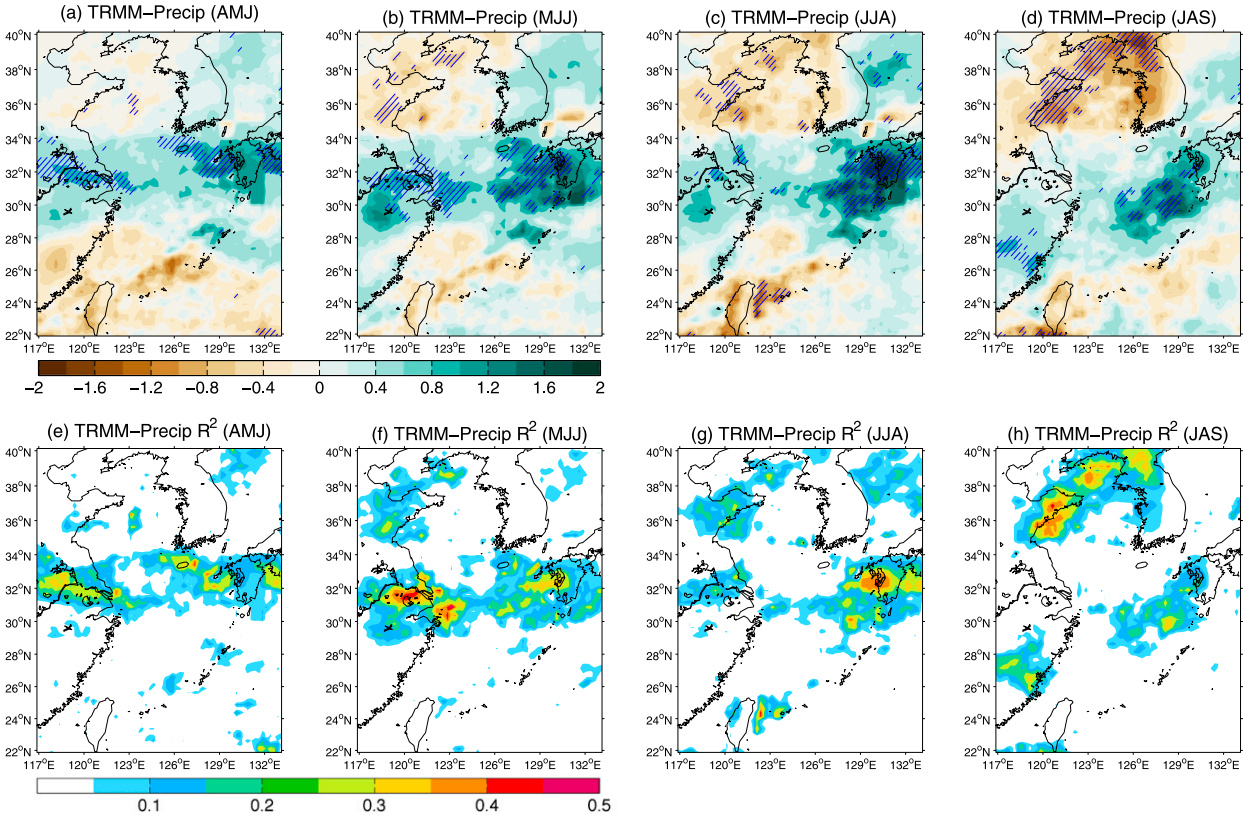

FIG. 7. (a)–(d) Simultaneous and lagged regressions of the seasonal-mean TRMM precipitation (mm day^{-1}; 1998–2015) from AMJ to JAS against the AMJ-SSHG-MCA1 and (e)–(h) the corresponding coefficients of determination R^2 (i.e., the portion of total variance of precipitation explained by the AMJ-SSHG-MCA1). Hatching indicates statistical significance at the 95% confidence level.

In response to the cold SST anomalies in MJJ, total precipitation indeed shows a zonal belt of positive anomalies in JJA (Fig. 9e; the MJJ response is very similar) and a unique center of positive anomalies over the central ECS in JAS (Fig. 9f), very similar to the TRMM-observation-based results (Figs. 7c,d). Furthermore, changes of the convective precipitation contribute little to the total precipitation response in most areas, except for eastern China (Figs. 9g,h). It is worth noting that the suppressed precipitation signals shown in Figs. 7c and 7d disappear, indicating a low robustness of such response. We also found that the precipitation regressions against the time series of SST anomalies area-averaged in the Japan/East Sea, however, do not show any significant responses (not shown).

The results so far point out a robust enhancement of rainfall from the Yangtze River delta to Kyushu in early summer (MJJ–JJA) and over the central ECS in late summer (JAS) driven by the offshore shift of the Kuroshio and the resultant cold SST anomalies in the northern ECS. A question might arise as to whether there is local atmospheric circulation variation in early summer that regulates both the Kuroshio path and precipitation, since Nakamura et al. (2015) suggest that the Kuroshio path state can be altered by local surface wind forcing. An inspection of local SLP (Fig. S5), however, shows that the lateral shift of the Kuroshio is not accompanied by any significant change in the local surface circulation. We also examined the simultaneous regression patterns of precipitation during MJJ-to-JAS against the western Pacific subtropical high (WPSH) index (Wang et al. 2013; highly correlating with the EASM indices) and the first two leading PCs of the tropical Pacific SST, respectively. We found that none of them resembles the precipitation response presented here. The correlation coefficients of the AMJ-SSHG-MCA1 with the WPSH index, the PC1, and the PC2 of the tropical Pacific SST in AMJ are 0.06, 0.17, and 0.02, respectively. Therefore, it further confirms that the precipitation is substantially affected by the lateral shift of the Kuroshio rather than either the large-scale EASM variation or the remote forcing of ENSO.

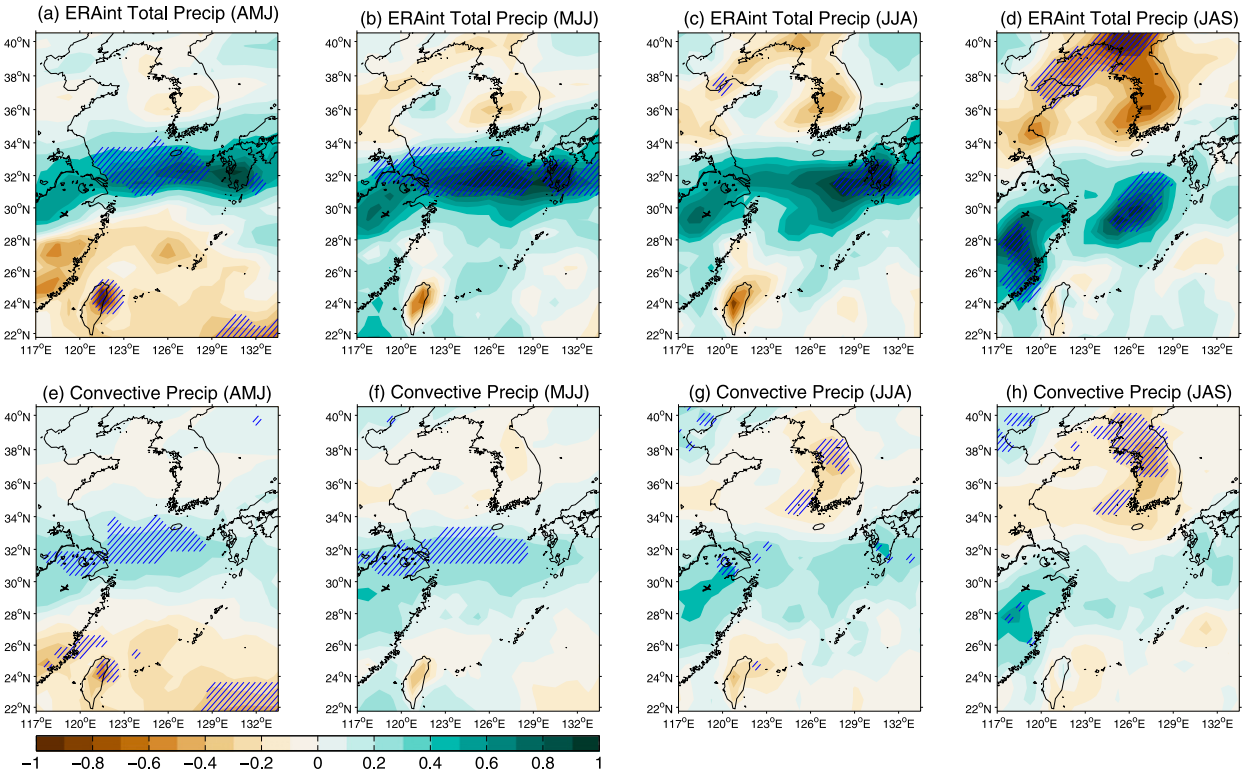

FIG. 8. As in Fig. 7, but for (a)–(d) the total precipitation and (e)–(h) the convective precipitation taken from the ERA-Interim product (mm day^{-1}; 1994–2015). Note the color bar range different from Fig. 7.

4. Possible mechanisms

a. *Contribution to the anomalous moisture flux convergence: Monthly-mean anomalies versus transient eddies*

Physical processes responsible for the summertime precipitation anomalies in response to the offshore shift of the Kuroshio are analyzed from the perspective of the atmospheric moisture balance. Figure 10 (first row) shows that the higher-than-normal precipitation in summer (Figs. 8a–d) is not balanced to the local surface evaporation change. Therefore, the moisture supply for the increased precipitation primarily comes from the lateral moisture flux convergence. As can be seen from Fig. 10 (second row), the spatial distribution of positive anomalies of total lateral moisture flux convergence ($\mathrm{ConQ}^{\mathrm{total}}$) well coincides with that of PmE, with a similar zonal-belt structure during AMJ–JJA and a well-defined anomaly center over the central ECS in JAS. According to Eq. (2), $\mathrm{ConQ}^{\mathrm{total}}$ can be broken down into a component due to the mean-flow moisture flux ($\mathrm{ConQ}^{\mathrm{mean}}$) and a component due to the transient eddy moisture flux ($\mathrm{ConQ}^{\mathrm{eddy}}$). The last two rows of Fig. 10 clearly show that the large positive anomalies of $\mathrm{ConQ}^{\mathrm{mean}}$ dominate the corresponding change of $\mathrm{ConQ}^{\mathrm{total}}$ during AMJ–JJA, whereas the positive anomaly center of $\mathrm{ConQ}^{\mathrm{total}}$ over the central ECS exclusively emerges from $\mathrm{ConQ}^{\mathrm{eddy}}$ in JAS. Interestingly, it seems that the effect of transient eddies particularly shows up in JAS, manifested as the additional significant anomalies appearing to the northwest over the Yellow Sea, which in turn contradict the effect of mean flow to some degree.

Therefore, the moisture budget analysis illuminates that the moisture supply for the increased precipitation from the Yangtze River delta to Kyushu in early summer (MJJ–JJA) and over the central ECS in late summer (JAS) come from the different processes (i.e., the mean-flow moisture flux convergence and the transient eddy moisture flux convergence, respectively). In the following subsections, we will further discuss the underlying different processes.

b. *Modulation on the mei-yu–baiu front during mid-May–June*

According to Eq. (4), we further split $\mathrm{ConQ}^{\mathrm{mean}}$ into the dynamic and thermodynamic contributions to the interannual variations of the mass convergence term ($\mathrm{ConQ}^{\mathrm{mean}}_{\mathrm{Div}}$) and the moisture advection term ($\mathrm{ConQ}^{\mathrm{mean}}_{\mathrm{Adv}}$). Figure 11 shows the decomposition for MJJ, and a similar

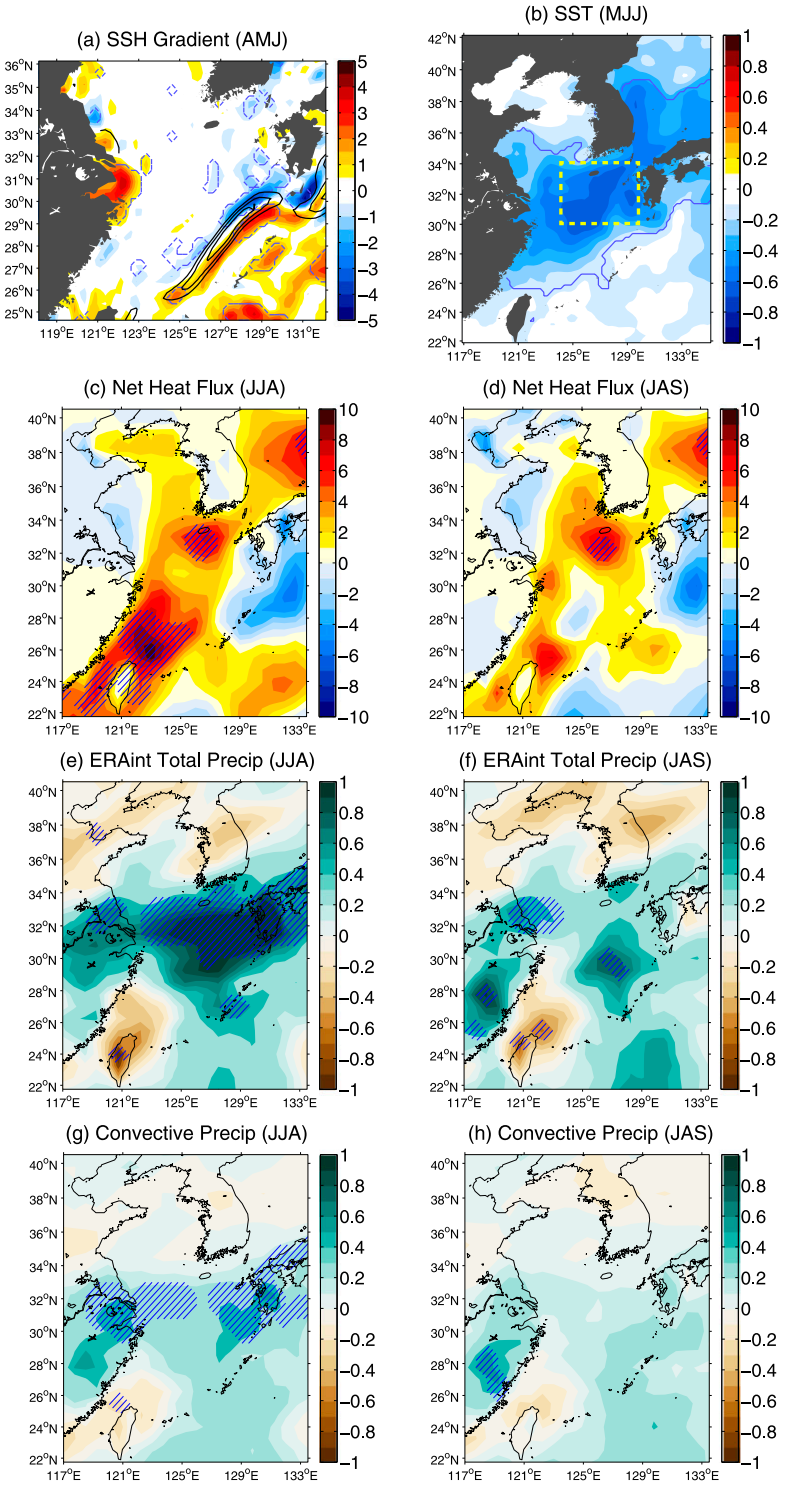

FIG. 9. Regressions of the seasonal-mean anomalies of (a) the AMJ SSH gradient [cm (100 km)$^{-1}$], (b) the MJJ SST (°C), (c),(d) net heat flux (W m^{-2}; positive is downward), (e),(f) the total precipitation, and (g),(h) the convective precipitation (mm day^{-1}) in JJA and JAS against the time series of MJJ SST anomalies area-averaged in the northern ECS. The box in (b) signifies the boundary of 30.125°–34.125°N, 124.625°–130.125°E used for the SST average. Hatched areas indicate statistical significance at the 95% confidence level. Precipitation data are taken from the ERA-Interim product (1994–2015). Note that to keep the sign of SST anomaly negative as same as in Fig. 3, we reversed the original SST time series.

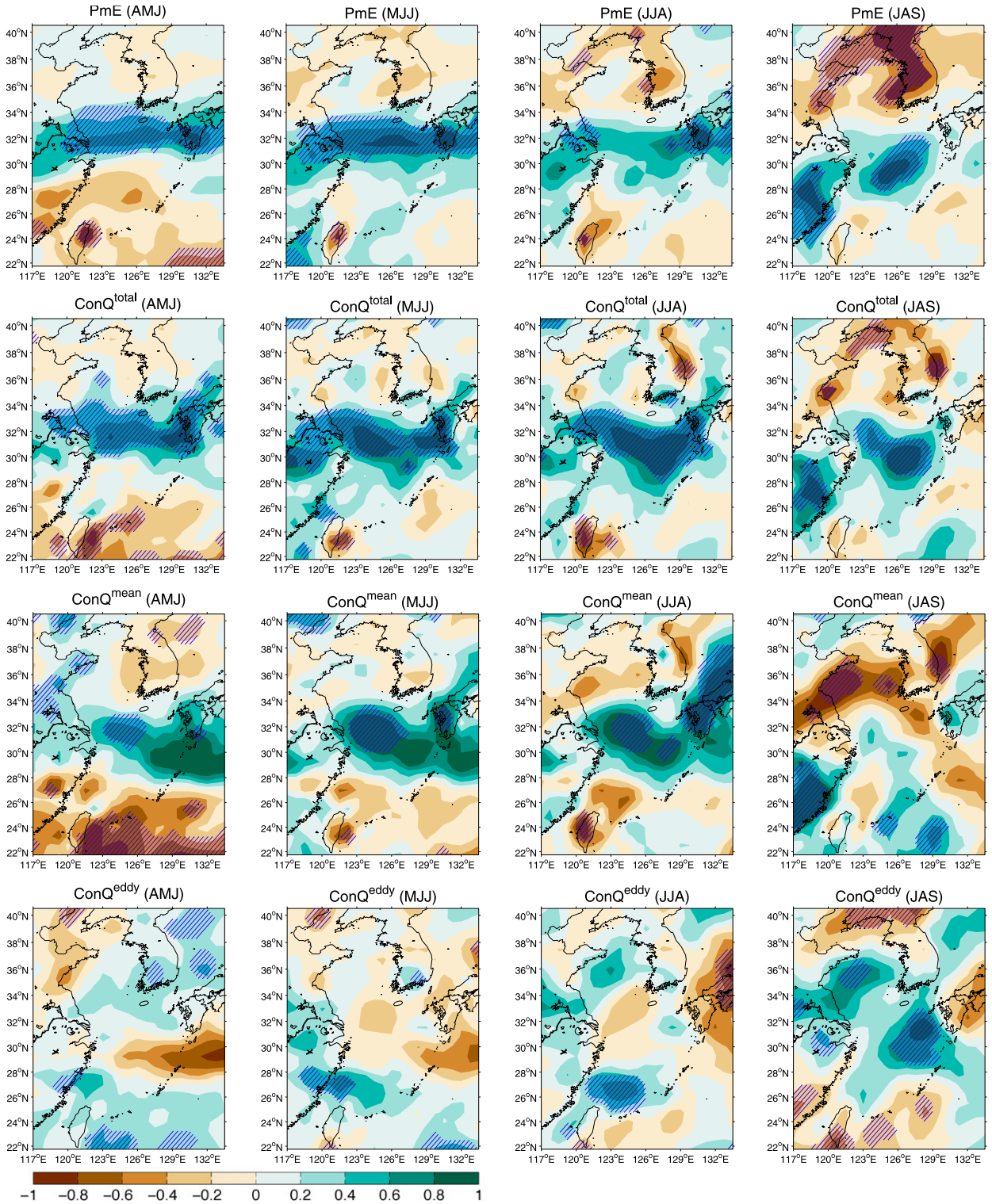

FIG. 10. Simultaneous and lagged regressions of the seasonal-mean column-integrated (from 100 hPa to the surface) moisture budget terms from (left) AMJ to (right) JAS against the AMJ-SSHG-MCA1: (top) precipitation minus evaporation, (second row) total lateral moisture flux convergence and its two components due to (third row) the monthly mean flow moisture flux and (bottom) the submonthly transient eddy moisture flux. Hatching areas indicate statistical significance at the 90% confidence level. Unit is mm day^{-1}. The moisture budget terms are calculated using the ERA-Interim product (1994–2015).

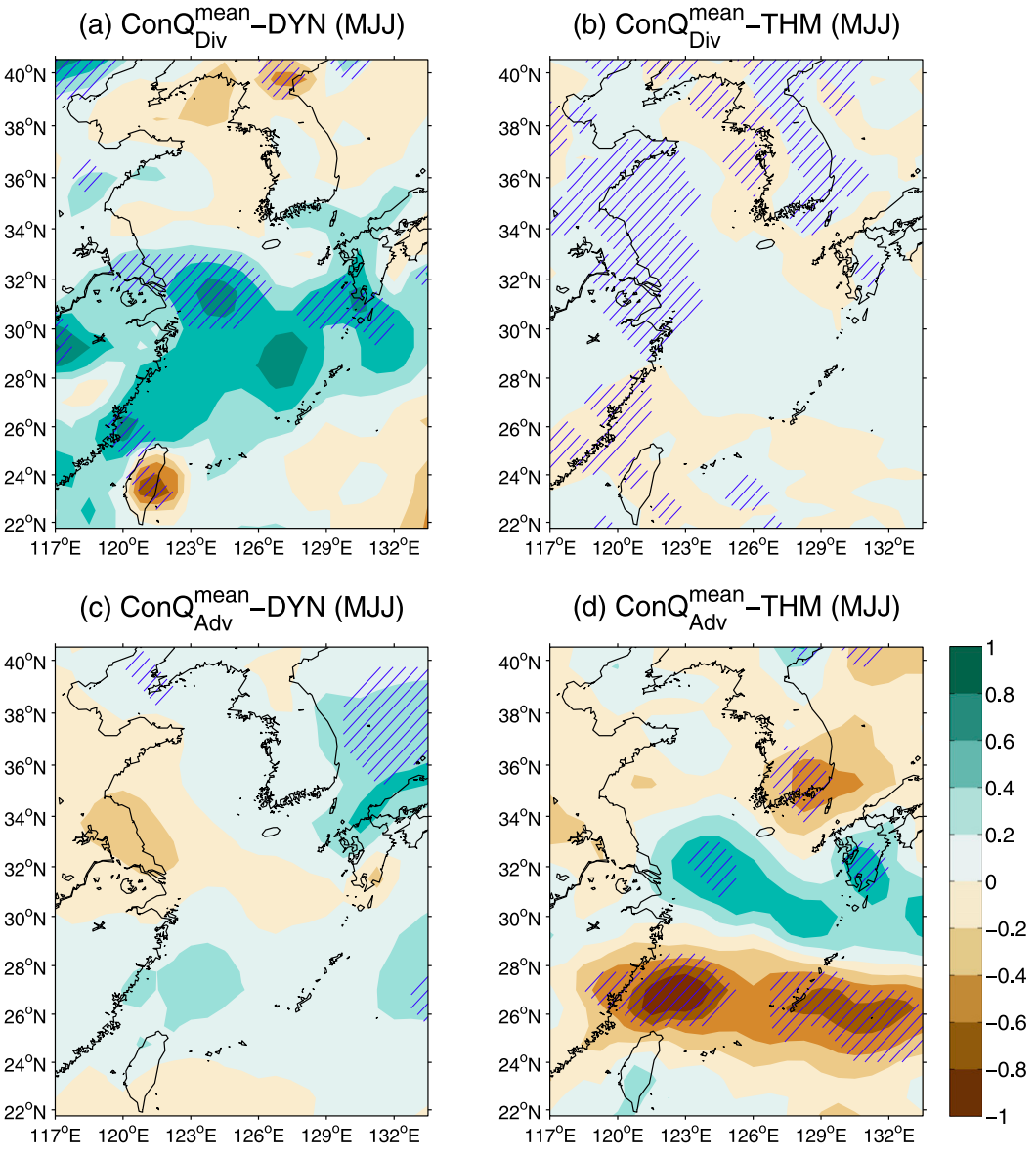

FIG. 11. As in Fig. 10, but for the regressions of the MJJ column-integrated (a) dynamic and (b) thermodynamic contributions to the interannual variation of the moisture convergence by divergent mean flow. (c),(d) As in (a) and (b), respectively, but for the mean-flow advection of moisture.

result for JJA is obtained (not shown). It can be clearly seen that a combination of dynamical (anomalous wind) contribution to the mass convergence term (Fig. 11a) and thermodynamic (anomalous humidity gradient) contribution to the moisture advection term (Fig. 11d) lead to the increase in ConQ^{mean} and precipitation from the Yangtze River delta to Kyushu. Particularly, the dynamical contribution plays a more important role than the thermodynamic contribution, except for Kyushu where both of them seem to be comparable. By contrast, the other two components have little contribution to ConQ^{mean} (Figs. 11b,c).

Furthermore, Fig. 12a reveals that the anomalous mass (wind) convergence (Fig. 11a) dynamically coincides with the anomalous ascent motion that is well collocated with the increased rain belt. It also shows that the anomalous upward pressure velocity at 500 hPa substantially shifts to the north of its climatological peak by roughly 2° of latitude. In addition, Fig. 12b reveals a significant strengthening of the poleward humidity gradient in the lower troposphere, which is induced by a significant reduction of humidity in the northern half of the domain (Fig. S6) and primarily leads to the corresponding increase in the anomalous moisture advection

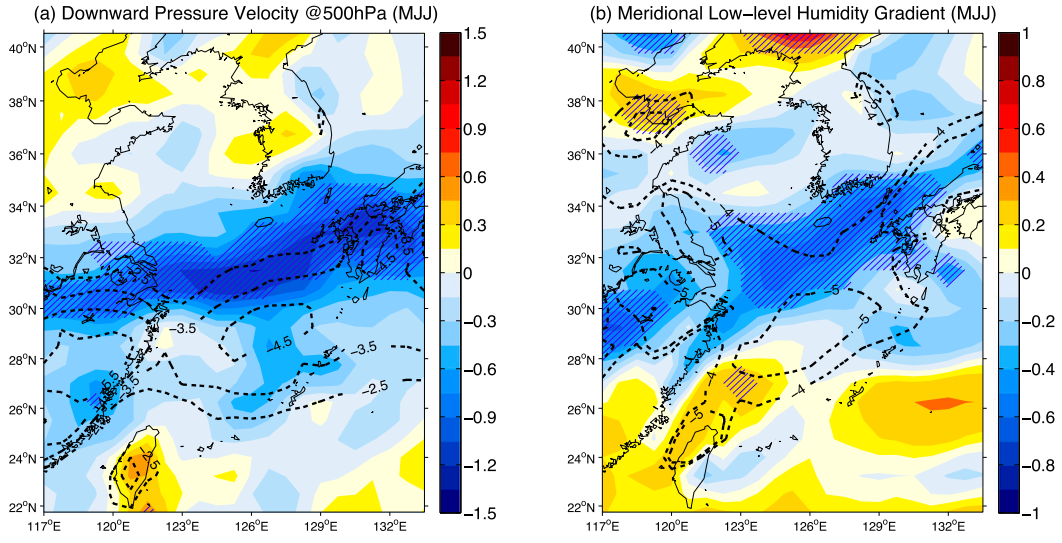

FIG. 12. As in Fig. 10, but for the regressions of (a) the MJJ downward pressure velocity (Pa s^{-1}; negative is upward) at 500 hPa and (b) the MJJ poleward gradient of the mass-weighted vertical-mean humidity over 1000–850 hPa [10^{-1} g kg^{-1} (100 km)$^{-1}$]. Dashed contours signify the corresponding climatology.

(Fig. 11d). This is understandable in the context of the large cold SST anomalies in the northern ECS that lower the evaporation (cf. Fig. 4 for turbulent heat flux). However, there seems to be a paradox that the anomalous ascent motion is accompanied with the cold SST anomalies. Sasaki and Yamada (2018) also show that the cold SST anomalies over the continental shelf are associated with the anomalous wind convergence over the central ECS, and the corresponding increased rainfall in June presumably results from the extratropical cyclone change. As for the present result, however, the precipitation response pattern is quite different from Sasaki and Yamada (2018), and its zonally elongated structure is reminiscent of the large-scale mei-yu–baiu rainband that has a frontal characteristic, the so-called mei-yu–baiu front (e.g., Ninomiya and Shibagaki 2007). Given this fact, we hypothesize that the offshore shift of the Kuroshio and the resultant cold SST anomalies in the northern ECS enhance the early-summer rainfall from the Yangtze River delta to Kyushu by modifying the seasonal northward migration of the mei-yu–baiu front.

To test the above hypothesis, we examined changes in the mei-yu–baiu front during AMJ–JJA associated with the lateral shift of the Kuroshio in AMJ. Here the mei-yu–baiu front is identified by the meridional (poleward) gradient of the mass-weighted vertical-mean equivalent potential temperature (EPT; a thermodynamic variable involving both temperature and humidity) in the lower troposphere (925–700 hPa), following Tomita et al. (2011). As can be seen from Figs. 13a–c, the lower-tropospheric EPT regressions exhibit a strengthening of significant negative anomalies in the northern half of the domain from AMJ to JJA, consistent with the evolution of cold SST anomalies (Fig. 3). Indeed, the vertical profile exhibits that the significant negative anomalies of EPT showing up at 31°N near the surface has a northward tilted structure, with the maximum at the near surface (925 hPa), which reflects the prominent cooling by ocean (Fig. 14). Correspondingly, the regressions of the poleward EPT gradient show an anomalous east–west front (i.e., the elongated band of negative anomalies, with the localized center over the northern ECS; colors in Figs. 13d–f). Comparing with the climatology, which well depicts the northward migration of the mei-yu–baiu front (dashed contours in Figs. 13d–f), such change indicates that when the Kuroshio shifts offshore in late spring, the mei-yu–baiu front is enhanced and moves to the northern ECS earlier than at its climatological-mean pace. As a result, rainfall over the Yangtze River delta and Kyushu is likely to be higher than normal in early summer.

We further scrutinized changes in the migration of the daily mei-yu–baiu front by compositing the daily zonal mean of poleward EPT gradient (over 120°–132°E) under the condition of the Kuroshio offshore–onshore shift. Here we focused on the offshore (onshore) shift of the AMJ Kuroshio, identified as the years when the AMJ-SSHG-MCA1 is greater (lower) than the top (bottom) 25th percentile (i.e., each case contains one-fourth of the total samples). As for the climatology, Fig. 15 (gray shading) shows that the mei-yu–baiu front stays within 28°–29°N during May and early June, in

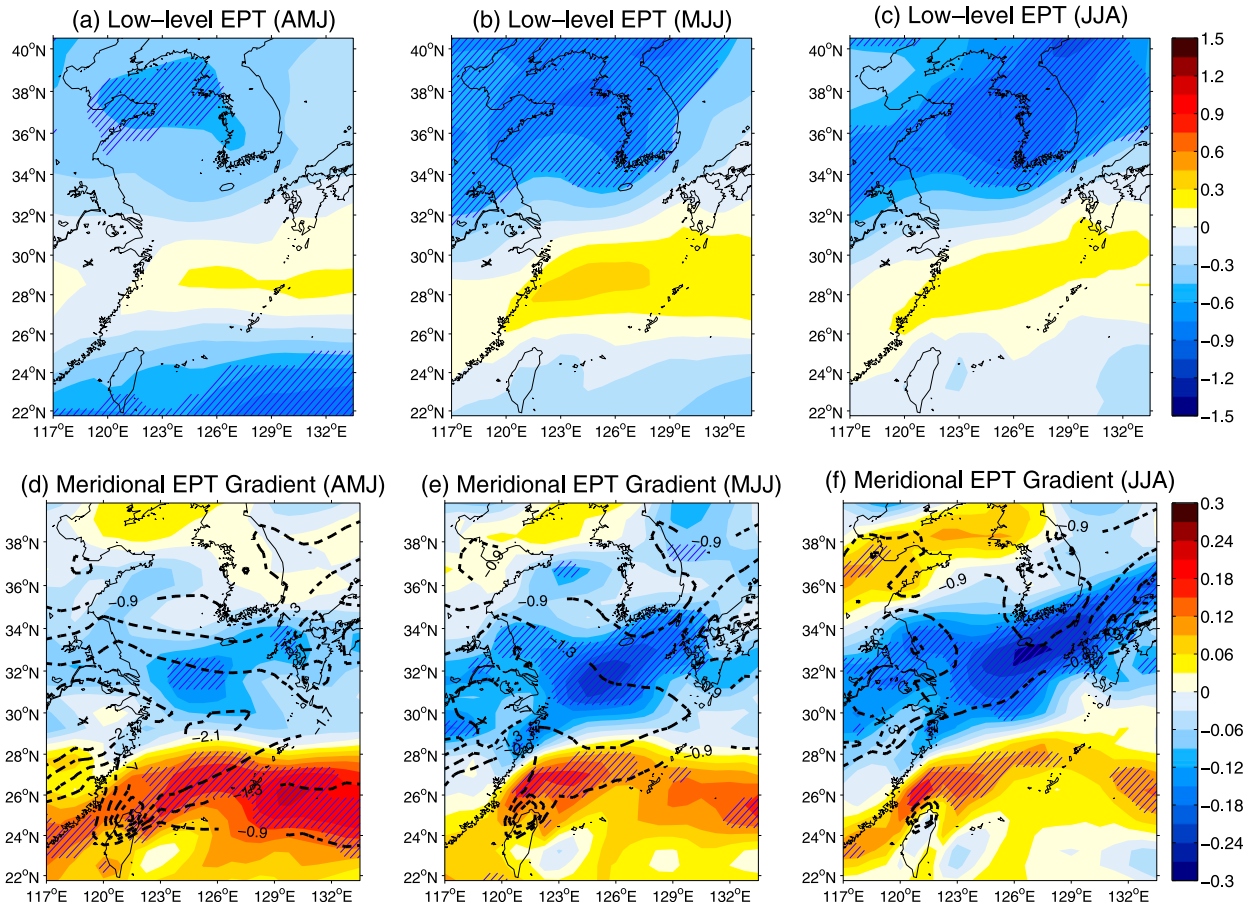

FIG. 13. As in Fig. 10, but for the regressions of (a)–(c) the lower-tropospheric equivalent potential temperature (EPT; K), which is derived from the mass-weighted vertical average of EPT over 925–700 hPa, and (d)–(f) the poleward gradient of the lower-tropospheric EPT [K (100 km)$^{-1}$], which represents the mei-yu–baiu front. Dashed contours in (d)–(f) signify the corresponding climatology.

correspondence with the rainband over southern China and the Kuroshio warm tongue in the ECS (not shown). Then, the rapid northward migration from 29° to 33°N occurs until mid-July, generally consistent with previous studies (e.g., Wang and LinHo 2002; Tomita et al. 2011; Xu et al. 2018). However, when the Kuroshio shifts offshore, the mei-yu–baiu front indeed substantially shifts to north of its climatological location by ~2° of latitude (i.e., staying within 30°–32°N) during mid-May–mid-June (see yellow dots with circles in Fig. 15). In other word, the northward migration of the mei-yu–baiu front, with an earlier start (roughly in mid-May), is slower than normal. Under the condition of the Kuroshio onshore shift, result seems to be opposite, such that the northward migration becomes faster than normal, with a somewhat later start.

It is expected that the slower-than-normal northward migration of the mei-yu–baiu front may prolong the local rainy season in the Yangtze River delta and Kyushu and thus bring more precipitation therein. This can be seen from Fig. 16, which shows the composites of daily precipitation area-averaged over the Yangtze River delta (30°–33°N, 118°–122°E) and Kyushu (30°–34°N, 129°–132°E) for the offshore–onshore shift of the AMJ Kuroshio. Both the TRMM and ERA-Interim results clearly present the significant increase of precipitation over both areas during mid-May–mid-June, when the mei-yu–baiu front arrives there earlier and migrates more slowly under the condition of the Kuroshio offshore shift (as shown in Fig. 15). It also seems that the precipitation response over the Kyushu is slightly more robust than that over the Yangtze River delta and more sensitive to the offshore shift than the onshore shift of the Kuroshio.

In general, the above analyses suggest that the offshore shift of the Kuroshio and the resultant cold SST anomalies in the northern ECS are likely to be conducive to the earlier arrival of the mei-yu–baiu front at 30°–32°N and its slower northward movement, which may prolong the local rainy season and thus leads to the

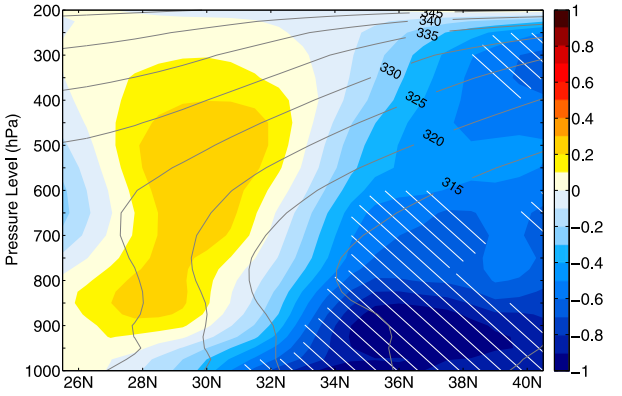

FIG. 14. Vertical profile of regressions of the zonal-mean (120°–130°E) EPT (K) in JJA against the AMJ-SSHG-MCA1, along with the corresponding climatology (gray contours). Hatched areas indicate statistical significance at the 90% confidence level.

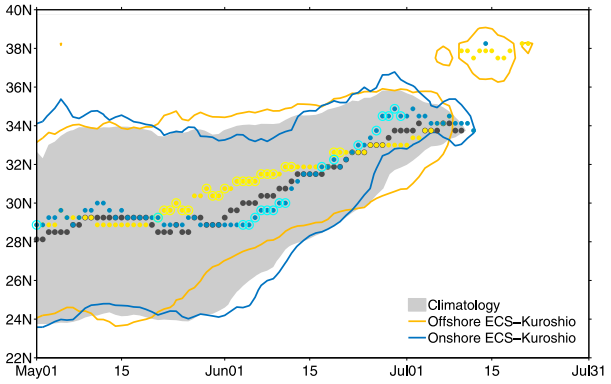

FIG. 15. Time–latitude section of the poleward gradient of the lower-tropospheric EPT zonally averaged over 120°–132°E illustrating the seasonal migration of the mei-yu–baiu front. Gray shading denotes the climatology lower than $-1.2\,\mathrm{K}\ (100\,\mathrm{km})^{-1}$, and yellow (blue) line denotes the composite under the offshore (onshore) shift of the AMJ Kuroshio. Black, yellow, and blue dots signify the median latitude of the meridional EPT gradient lower than $-1.2\,\mathrm{K}\ (100\,\mathrm{km})^{-1}$ outlined in the gray shading and yellow and blue lines, respectively. Dots with circles signify the deviation from climatology that is statistically significant at the 90% confidence level based on the Monte Carlo test. The meridional EPT gradient is smoothed with 2-week running mean. The abscissa denotes the central calendar date of the running window.

above-normal precipitation from the Yangtze River delta to Kyushu in early summer.

c. *Role of extratropical cyclones*

Recalling that a large part of the anomalous precipitation-minus-evaporation value in late summer (JAS) is contributed by the anomalous transient eddy moisture flux convergence (Fig. 10), which implies the potential influence of the Kuroshio lateral shift on the extratropical cyclones. Given that a comparison of Fig. 8d with Fig. 9f suggests a high robustness of the increased precipitation over the central ECS, here we discussed its causative process therein.

An important process by which the Kuroshio variation affects the extratropical cyclones lies in the change of atmospheric baroclinicity, which provides the baroclinic source for the growth of transient eddies (e.g., Gan and Wu 2013). We estimated the near-surface baroclinicity by the maximum Eady growth rate (Lindzen and Farrell 1980), that is, $\sigma_{\mathrm{Eady}} = 0.31g(N\overline{\theta})^{-1}|\nabla\overline{\theta}|$, where N denotes the Brunt–Väisälä frequency, $\overline{\theta}$ is the average of monthly mean potential temperature between two adjacent pressure levels, and the other notations are standard. We also employed the F diagnostic to evaluate the atmospheric fronts embedded in the extratropical cyclones. According to Parfitt et al. (2017), the nondimensional F for a specific pressure level p is $F_p = \zeta_p|\nabla T_p|/(f|\nabla T|_o)$, where ζ is the relative vorticity, ∇T is the horizontal gradient of temperature, f is the Coriolis parameter at the relevant latitude, and $|\nabla T|_o = 0.45\,\mathrm{K}\ (100\,\mathrm{km})^{-1}$. Parfitt et al. (2017) used $F \geq 1$ to detect all atmospheric fronts in winter. Here we calculated F at 850 hPa (F_{850}) based on the daily fields and masked frontal grid points as the relatively strong atmospheric fronts with the criteria of $F_{850} > 2$ and a minimum extension of three neighboring frontal points.

Figure 17 clearly suggests that the offshore shift of the Kuroshio strengthens the near-surface baroclinicity and the associated strong atmospheric fronts embedded in the extratropical cyclones over the central ECS in JAS, which in turn enhances the local precipitation. Specifically, associated with the AMJ Kuroshio offshore shift, change in the 925-hPa σ_{Eady} shows a southwest–northeast-tilted structure of significant positive anomalies nearly above the Kuroshio warm tongue (Fig. 17a). Further inspection shows that the increased σ_{Eady} is dominated by the enhancement of the horizontal temperature gradient (not shown), which is likely due to the cooling of atmosphere by the cold SST anomalies (cf. Fig. 4). The strengthening of the near-surface baroclinicity thus could fuel cyclones by offering more available potential energy. As expected, a similar band-like structure is also presented in the frequency of strong atmospheric fronts embedded in the extratropical cyclones, with a positive anomaly center located to slightly downstream of the positive σ_{Eady} anomaly in the central ECS (Fig. 17b). This displacement may be due to the time lag for the development of baroclinic eddies (Sasaki and Yamada 2018). We further composited the total precipitation associated with the strong atmospheric fronts passing over southwest of Kyushu

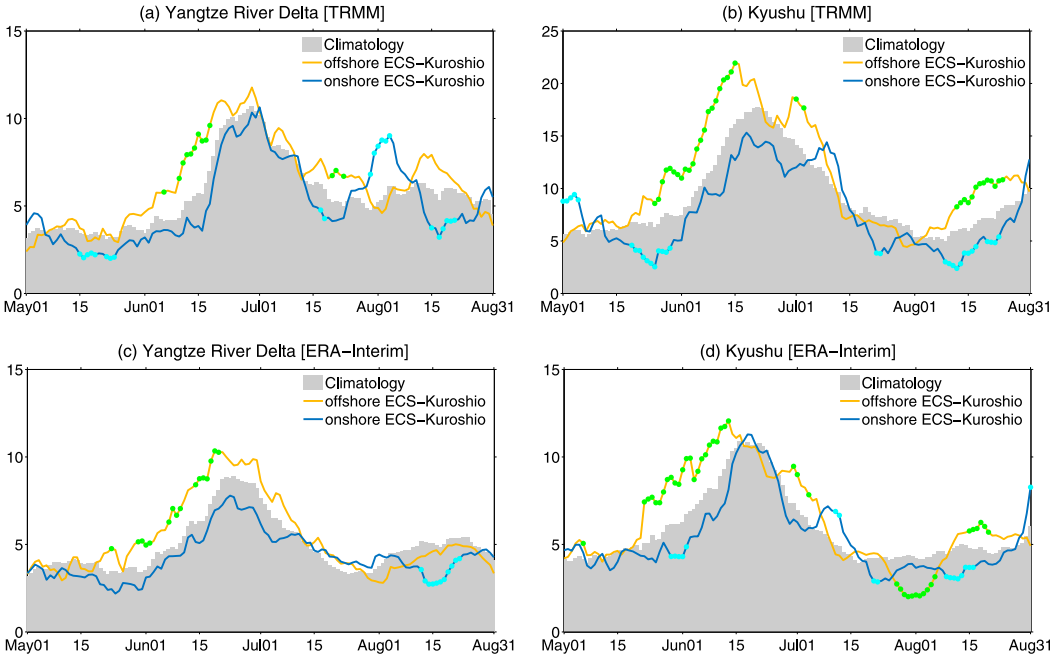

FIG. 16. Composites of daily precipitation (mm day^{-1}) area-averaged over the Yangtze River delta (30°–33°N, 118°–122°E) and Kyushu (30°–34°N, 129°–132°E) for the offshore–onshore shift of the AMJ Kuroshio, along with the corresponding climatology. Daily precipitation data are taken from (a),(b) the TRMM observations and (c),(d) the ERA-Interim . Dots signify a deviation from climatology that is statistically significant at the 90% confidence level based on the Monte Carlo test. Here the daily precipitation is smoothed with 2-week running mean. The abscissa denotes the central calendar date of the running window.

(see box in Fig. 17b). A confined center of increased frontal precipitation is clearly shown in the central ECS (Fig. 17c), which well coincides with the late-summer precipitation response to the Kuroshio offshore shift (cf. Fig. 8d). Note that, in sharp contrast to the above-mentioned responses in JAS, we found no significant positive anomalies of the near-surface baroclinicity and the atmospheric front frequency over the ECS in MJJ or JJA (not shown).

5. Summary and discussion

The present study investigated the interannual variability of the Kuroshio in the ECS and its impacts on the

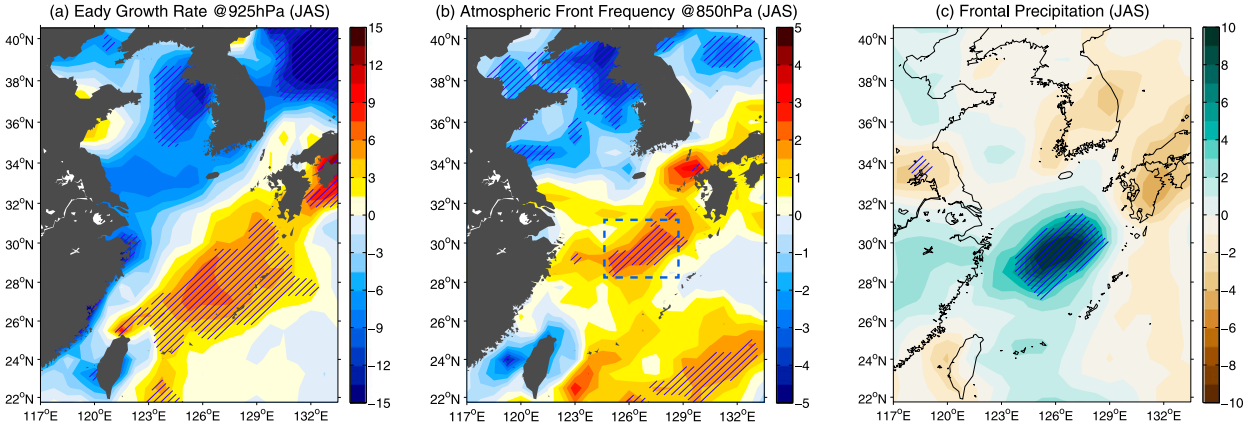

FIG. 17. Composite differences between the offshore and onshore shifts of the AMJ Kuroshio for (a) the maximum Eady growth rate ($\times 10^{-2}$ day^{-1}) at 925 hPa, (b) the frequency of the strong atmospheric fronts detected by $F_{850} > 2$, and (c) the ERA-Interim total precipitation (mm day^{-1}) associated with the strong atmospheric fronts passing over southwest of Kyushu [see box in (b)]. The frontal frequency is expressed as the percentage of the JAS period. Hatching areas indicate statistical significance at the 90% confidence level based on the Monte Carlo test.

continental SST as well as the summertime precipitation over the surrounding area. Based on the high-resolution satellite observations and the lagged MCA analysis, the results show that the dominant variation of the Kuroshio exhibits the offshore and onshore shifts of its main axis on interannual time scale (a period of about 3–4 years), and it is such a shift in late spring that has the most prominent influence on the marginal seas in summer. Particularly, the persistent offshore shift of the Kuroshio since late spring (AMJ) can result in the cold SST anomalies in the northern ECS and the Japan/East Sea until late summer (JAS), which correspondingly causes anomalous cooling of the overlying atmosphere. We found that the offshore shift of the Kuroshio leads to a significant weakening of the Tsushima Warm Current and the East Korea Warm Current, which in turn likely drives the cold SST anomalies due to the anomalous cold advection. The driving force of the lateral shift of the Kuroshio is beyond the scope of this study, but preliminary inspection shows that the offshore shift of the Kuroshio significantly correlates to a lower-than-normal SLP over the eastern subtropical North Pacific in late winter (JFM), which may imply a shrinking of the subtropical gyre of the North Pacific Ocean. Interestingly, such SLP change is further associated with the Arctic Oscillation rather than the North Pacific Oscillation.

When the Kuroshio shifts offshore in AMJ, precipitation is found to significantly increase over a zonal band from the Yangtze River delta to Kyushu in early summer (MJJ–JJA) and over the central ECS in late summer (JAS). Particularly, the TRMM data show that the interannual variability of the Kuroshio lateral shift in AMJ can explain about 40% and 35% of total variance of precipitation over the Yangtze River delta in MJJ and over Kyushu in JJA, respectively. It is suggested that the cold SST anomalies in the northern ECS rather than the Japan/East Sea induced by the Kuroshio offshore shift is a key driver for such enhancement of precipitation. We also confirmed that the significant response of precipitation to the lateral shift of the Kuroshio is not contaminated by either the large-scale EASM variation or the remote forcing of ENSO. In fact, Fujibe (2015) has reported that there is negative correlation between extreme precipitation/total precipitation amount over Kyushu and SST in its surrounding area in summer, consistent with the present results. Our study, however, further indicates that interannual variations of the Kuroshio lateral shift and SST in the northern ECS may provide predictive values for the precipitation variation over Kyushu and the Yangtze River delta. This predictability is worth addressing in a future study.

Analysis of the moisture budget shows that the moisture supply for the increased precipitation from the Yangtze River delta to Kyushu in early summer and over the central ECS in late summer come from different processes (i.e., the mean-flow moisture flux convergence and the transient eddy moisture flux convergence, respectively). Particularly, further decomposition of the mean-flow moisture flux convergence suggests the dominant contribution from a combination of the anomalous mass (wind) convergence (dynamically coinciding with the anomalous ascent motion) and the mean advection of anomalous humidity gradient (primarily resulting from the strengthened poleward humidity gradient).

On the basis of the moisture budget results, we further proposed two different physical processes modulated by the lateral shift of the Kuroshio that are likely responsible for the distinct responses of precipitation in early summer and late summer, respectively. On the one hand, the cold SST anomalies in the northern ECS induced by the Kuroshio offshore shift are likely conducive to the earlier arrival of the mei-yu–baiu front at 30°–32°N and its slower northward movement, which may prolong the local rainy season and thus leads to the above-normal precipitation from the Yangtze River delta to Kyushu in early summer (MJJ–JJA). On the other hand, the persistent cold SST anomalies in late summer (JAS) strengthen the near-surface baroclinicity and the associated strong atmospheric fronts embedded in the extratropical cyclones over the central ECS, which in turn enhances the local precipitation. Note that we do not rule out a contribution of rainfall brought by the extratropical cyclones to the increased precipitation over Kyushu in August during the period of the Kuroshio offshore shift, which however seems to be only captured by the high-spatial-resolution TRMM product (cf. Fig. 16b).

Our results reveal the role of interannual variations of the Kuroshio and the northern ECS SST in the precipitation variation from the Yangtze River delta to Kyushu in MJJ–JJA, through the modulation on the large-scale mei-yu–baiu front. This is different from the findings of Sasaki and Yamada (2018), who highlight that the central–southern ECS SST variation affects the precipitation over the central ECS in June by altering the extratropical cyclones. Indeed, we found that the simultaneous regression patterns of total precipitation against the time series of SST anomalies area-averaged in the northern ECS (see box in Fig. 9b) and the central–southern ECS (25.625°–30.875°N, 121.125°–129.125°E) in June are similar to Fig. 9e of the present study and Fig. 7a of Sasaki and Yamada (2018), respectively (not shown). This fact confirms both studies' results and implies a sensitivity of regional rainfall to the

position of local SST anomalies. However, the correlation coefficient between the PC1 of the entire ECS SST and the SST time series for the northern ECS in June is higher than the case for the central–southern ECS (0.87 vs 0.77), suggesting that the dominant SST variability in the ECS is more concentrated in the northern ECS. Furthermore, the dominant interannual variability of the Kuroshio lateral shift (i.e., PC1 of the SSH gradient) in May is found to explain about 30% of the total SST variance in the northern ECS in June.

Acknowledgments. We appreciate three anonymous reviewers for their thoughtful and constructive comments. This work is supported by the National Key Research and Development Program of China (2016YFA0601804), the National Natural Science Foundation of China (NSFC) Projects (91858102, 41490643, 41490640, 41506009, U1606402) and the OUC–WHOI joint research program (21366).

REFERENCES

Andres, M., Y.-O. Kwon, and J. Yang, 2011: Observations of the Kuroshio's barotropic and baroclinic responses to basin-wide wind forcing. *J. Geophys. Res.*, **116**, C04011, https://doi.org/10.1029/2010JC006863.

Czaja, A., and C. Frankignoul, 1999: Influence of the North Atlantic SST anomalies on the atmospheric circulation. *Geophys. Res. Lett.*, **26**, 2969–2972, https://doi.org/10.1029/1999GL900613.

——, and ——, 2002: Observed impact of Atlantic SST anomalies on the North Atlantic oscillation. *J. Climate*, **15**, 606–623, https://doi.org/10.1175/1520-0442(2002)015<0606:OIOASA>2.0.CO;2.

Dee, D. P., and Coauthors, 2011: The ERA-Interim reanalysis: Configuration and performance of the data assimilation system. *Quart. J. Roy. Meteor. Soc.*, **137**, 553–597, https://doi.org/10.1002/qj.828.

Ding, Y., and J. C. L. Chan, 2005: The East Asian summer monsoon: An overview. *Meteor. Atmos. Phys.*, **89**, 117–142, https://doi.org/10.1007/s00703-005-0125-z.

Ducet, N., P.-Y. Le Traon, and G. Reverdin, 2000: Global high-resolution mapping of ocean circulation from TOPEX/Poseidon and ERS-1 and -2. *J. Geophys. Res.*, **105**, 19 477–19 498, https://doi.org/10.1029/2000JC900063.

Frankignoul, C., N. Sennéchael, Y.-O. Kwon, and M. A. Alexander, 2011: Influence of the meridional shifts of the Kuroshio and the Oyashio Extensions on the atmospheric circulation. *J. Climate*, **24**, 762–777, https://doi.org/10.1175/2010JCLI3731.1.

Fujibe, F., 2015: Relationship between interannual variations of extreme hourly precipitation and air/sea-surface temperature in Japan. *SOLA*, **11**, 5–9, https://doi.org/10.2151/sola.2015-002.

Gan, B., and L. Wu, 2012: Modulation of atmospheric response to North Pacific SST anomalies under global warming: A statistical assessment. *J. Climate*, **25**, 6554–6566, https://doi.org/10.1175/JCLI-D-11-00493.1.

——, and ——, 2013: Seasonal and long-term coupling between wintertime storm tracks and sea surface temperature in the North Pacific. *J. Climate*, **26**, 6123–6136, https://doi.org/10.1175/JCLI-D-12-00724.1.

——, and ——, 2015: Feedbacks of sea surface temperature to wintertime storm tracks in the North Atlantic. *J. Climate*, **28**, 306–323, https://doi.org/10.1175/JCLI-D-13-00719.1.

Guo, X., Y. Miyazawa, and T. Yamagata, 2006: The Kuroshio onshore intrusion along the shelf break of the East China Sea: The origin of the Tsushima Warm Current. *J. Phys. Oceanogr.*, **36**, 2205–2231, https://doi.org/10.1175/JPO2976.1.

Hsueh, Y., 2000: The Kuroshio in the East China Sea. *J. Mar. Syst.*, **24**, 131–139, https://doi.org/10.1016/S0924-7963(99)00083-4.

Huang, R., W. Chen, B. Yang, and R. Zhang, 2004: Recent advances in studies of the interaction between the East Asian winter and summer monsoons and ENSO cycle. *Adv. Atmos. Sci.*, **21**, 407–424, https://doi.org/10.1007/BF02915568.

Huffman, G. J., and Coauthors, 2007: The TRMM Multisatellite Precipitation Analysis: Quasi-global, multiyear, combined-sensor precipitation estimates at fine scales. *J. Hydrometeor.*, **8**, 38–55, https://doi.org/10.1175/JHM560.1.

Ichikawa, H., and R. C. Beardsley, 2002: The current system in the Yellow and East China Seas. *J. Oceanogr.*, **58**, 77–92, https://doi.org/10.1023/A:1015876701363.

Kelly, K. A., R. J. Small, R. M. Samelson, B. Qiu, T. M. Joyce, Y.-O. Kwon, and M. F. Cronin, 2010: Western boundary currents and frontal air–sea interaction: Gulf Stream and Kuroshio Extension. *J. Climate*, **23**, 5644–5667, https://doi.org/10.1175/2010JCLI3346.1.

Kunoki, S., and Coauthors, 2015: Oceanic influence on the Baiu frontal zone in the East China Sea. *J. Geophys. Res.*, **120**, 449–463, https://doi.org/10.1002/2014JD022234.

Kuwano-Yoshida, A., and S. Minobe, 2017: Storm-track response to SST fronts in the northwestern Pacific region in an AGCM. *J. Climate*, **30**, 1081–1102, https://doi.org/10.1175/JCLI-D-16-0331.1.

Kwon, M., J.-G. Jhun, B. Wang, S.-I. An, and J.-S. Kug, 2005: Decadal change in relationship between East Asian and WNP summer monsoons. *Geophys. Res. Lett.*, **32**, L16709, https://doi.org/10.1029/2005GL023026.

Kwon, Y.-O., and T. M. Joyce, 2013: Northern Hemisphere winter atmospheric transient eddy heat fluxes and the Gulf Stream and Kuroshio–Oyashio Extension variability. *J. Climate*, **26**, 9839–9859, https://doi.org/10.1175/JCLI-D-12-00647.1.

——, M. A. Alexander, N. A. Bond, C. Frankignoul, H. Nakamura, B. Qiu, and L. A. Thompson, 2010: Role of the Gulf Stream and Kuroshio–Oyashio systems in large-scale atmosphere–ocean interaction: A review. *J. Climate*, **23**, 3249–3281, https://doi.org/10.1175/2010JCLI3343.1.

Lindzen, R. S., and B. Farrell, 1980:A simple approximate result for the maximum growth rate of baroclinic instabilities. *J. Atmos. Sci.*, **37**, 1648–1654, https://doi.org/10.1175/1520-0469(1980)037<1648:ASARFT>2.0.CO;2.

——, and S. Nigam, 1987: On the role of sea surface temperature gradients in forcing low-level winds and convergence in the tropics. *J. Atmos. Sci.*, **44**, 2418–2436, https://doi.org/10.1175/1520-0469(1987)044<2418:OTROSS>2.0.CO;2.

Liu, J.-W., S.-P. Xie, S. Yang, and S.-P. Zhang, 2016: Low-cloud transitions across the Kuroshio Front in the East China Sea. *J. Climate*, **29**, 4429–4443, https://doi.org/10.1175/JCLI-D-15-0589.1.

Liu, Z., and J. Gan, 2012: Variability of the Kuroshio in the East China Sea derived from satellite altimetry data. *Deep-Sea Res. I*, **59**, 25–36, https://doi.org/10.1016/j.dsr.2011.10.008.

Ma, X., and Coauthors, 2015: Distant influence of Kuroshio eddies on North Pacific weather patterns? *Sci. Rep.*, **5**, 17785, https://doi.org/10.1038/srep17785.

Masunaga, R., H. Nakamura, T. Miyasaka, K. Nishii, and Y. Tanimoto, 2015: Separation of climatological imprints of the Kuroshio Extension and Oyashio fronts on the wintertime atmospheric boundary layer: Their sensitivity to SST resolution prescribed for atmospheric reanalysis. *J. Climate*, **28**, 1764–1787, https://doi.org/10.1175/JCLI-D-14-00314.1.

——, ——, ——, ——, and B. Qiu, 2016: Interannual modulations of oceanic imprints on the wintertime atmospheric boundary layer under the changing dynamical regimes of the Kuroshio Extension. *J. Climate*, **29**, 3273–3296, https://doi.org/10.1175/JCLI-D-15-0545.1.

Minobe, S., M. Miyashita, A. Kuwano-Yoshida, H. Tokinaga, and S.-P. Xie, 2010: Atmospheric response to the Gulf Stream: Seasonal variations. *J. Climate*, **23**, 3699–3719, https://doi.org/10.1175/2010JCLI3359.1.

Nakamura, Hirohiko, R. Hiranaka, D. Ambe, and T. Saito, 2015: Local wind effect on the Kuroshio path state of the southeastern coast of Kyushu. *J. Oceanogr.*, **71**, 575–596, https://doi.org/10.1007/s10872-015-0309-1.

Nakamura, Hisashi, T. Sampe, Y. Tanimoto, and A. Shimpo, 2004: Observed associations among storm tracks, jet streams and midlatitude oceanic fronts. *Earth's Climate: The Ocean–Atmosphere Interaction*, *Geophys. Monogr.*, Vol. 147, Amer. Geophys. Union, 329–345.

Newman, M., and Coauthors, 2016: The Pacific decadal oscillation, revisited. *J. Climate*, **29**, 4399–4427, https://doi.org/10.1175/JCLI-D-15-0508.1.

Ninomiya, K., and T. Murakami, 1987: The early summer rainy season (Baiu) over Japan. *Monsoon Meteorology*, C.-P. Chang, and T. N. Krishnamurti, Eds., Oxford University Press, 93–121.

——, and Y. Shibagaki, 2007: Multi-scale features of the Meiyu-Baiu front and associated precipitation systems. *J. Meteor. Soc. Japan*, **85B**, 103–122, https://doi.org/10.2151/jmsj.85B.103.

O'Reilly, C. H., and A. Czaja, 2015: The response of the Pacific storm track and atmospheric circulation to Kuroshio Extension variability. *Quart. J. Roy. Meteor. Soc.*, **141**, 52–66, https://doi.org/10.1002/qj.2334.

Parfitt, R., A. Czaja, and H. Seo, 2017: A simple diagnostic for the detection of atmospheric fronts. *Geophys. Res. Lett.*, **44**, 4351–4358, https://doi.org/10.1002/2017GL073662.

Révelard, A., C. Frankignoul, N. Sennechael, Y. O. Kwon, and B. Qiu, 2016: Influence of the decadal variability of the Kuroshio Extension on the atmospheric circulation in the cold season. *J. Climate*, **29**, 2123–2144, https://doi.org/10.1175/JCLI-D-15-0511.1.

Reynolds, R. W., T. M. Smith, C. Liu, D. B. Chelton, K. S. Casey, and M. G. Schlax, 2007: Daily high-resolution-blended analyses for sea surface temperature. *J. Climate*, **20**, 5473–5496, https://doi.org/10.1175/2007JCLI1824.1.

Sampe, T., and S.-P. Xie, 2010: Large-scale dynamics of the meiyu-baiu rainband: Environmental forcing by the westerly jet. *J. Climate*, **23**, 113–134, https://doi.org/10.1175/2009JCLI3128.1.

Sasaki, Y. N., and Y. Yamada, 2018: Atmospheric response to interannual variability of sea surface temperature front in the East China Sea in early summer. *Climate Dyn.*, **51**, 2509–2522, https://doi.org/10.1007/s00382-017-4025-y.

——, S. Minobe, T. Asai, and M. Inatsu, 2012: Influence of the Kuroshio in the East China Sea on the early summer (baiu) rain. *J. Climate*, **25**, 6627–6645, https://doi.org/10.1175/JCLI-D-11-00727.1.

Seager, R., and N. Henderson, 2013: Diagnostic computation of moisture budgets in the ERA-Interim reanalysis with reference to analysis of CMIP-archived atmospheric model data. *J. Climate*, **26**, 7876–7901, https://doi.org/10.1175/JCLI-D-13-00018.1.

Small, R. J., R. A. Tomas, and F. O. Bryan, 2014: Storm track response to ocean fronts in a global high-resolution climate model. *Climate Dyn.*, **43**, 805–828, https://doi.org/10.1007/s00382-013-1980-9.

Taguchi, B., H. Nakamura, M. Nonaka, N. Komori, A. Kuwano-Yoshida, K. Takaya, and A. Goto, 2012: Seasonal evolutions of atmospheric response to decadal SST anomalies in the North Pacific subarctic frontal zone: Observations and a coupled model simulation. *J. Climate*, **25**, 111–139, https://doi.org/10.1175/JCLI-D-11-00046.1.

Tao, S., and L. Chen, 1987: A review of recent research on the East Asian summer monsoon in China. *Monsoon Meteorology*, C.-P. Chang and T. N. Krishnamurti, Eds., Oxford University Press, 60–92.

Tokinaga, H., Y. Tanimoto, S.-P. Xie, T. Sampe, H. Tomita, and H. Ichikawa, 2009: Ocean frontal effects on the vertical development of clouds over the western North Pacific: In situ and satellite observations. *J. Climate*, **22**, 4241–4260, https://doi.org/10.1175/2009JCLI2763.1.

Tomita, T., T. Yamaura, and T. Hashimoto, 2011: Interannual variability of the Baiu season near Japan evaluated from the equivalent potential temperature. *J. Meteor. Soc. Japan*, **89**, 517–537, https://doi.org/10.2151/jmsj.2011-507.

Wang, B., and LinHo, 2002: Rainy season of the Asian–Pacific summer monsoon. *J. Climate*, **15**, 386–398, https://doi.org/10.1175/1520-0442(2002)015<0386:RSOTAP>2.0.CO;2.

——, B. Xiang, and J. Y. Lee, 2013: Subtropical high predictability establishes a promising way for monsoon and tropical storm predictions. *Proc. Natl. Acad. Sci. USA*, **110**, 2718–2722, https://doi.org/10.1073/pnas.1214626110.

Wei, Y., D. Huang, and X.-H. Zhu, 2013: Interannual to decadal variability of the Kuroshio Current in the East China Sea from 1955 to 2010 as indicated by in-situ hydrographic data. *J. Oceanogr.*, **69**, 571–589, https://doi.org/10.1007/s10872-013-0193-5.

Xie, S.-P., K. Hu, J. Hafner, H. Tokinaga, Y. Du, G. Huang, and T. Sampe, 2009: Indian Ocean capacitor effect on Indo–western Pacific climate during the summer following El Niño. *J. Climate*, **22**, 730–747, https://doi.org/10.1175/2008JCLI2544.1.

Xu, H., M. Xu, S.-P. Xie, and Y. Wang, 2011: Deep atmospheric response to the spring Kuroshio over the East China Sea. *J. Climate*, **24**, 4959–4972, https://doi.org/10.1175/JCLI-D-10-05034.1.

Xu, M., H. Xu, and H. Ren, 2018: Influence of Kuroshio SST front in the East China Sea on the climatological evolution of Meiyu rainband. *Climate Dyn.*, **50**, 1243–1266, https://doi.org/10.1007/s00382-017-3681-2.

Zhang, L. P., L. Wu, and B. Gan, 2013: Modes and mechanisms of global water vapor variability over the twentieth century. *J. Climate*, **26**, 5578–5593, https://doi.org/10.1175/JCLI-D-12-00585.1.

Zhang, L. Z., B. Gan, L. Wu, W. Cai, and H. Ma, 2018: Seasonal dependence of coupling between storm tracks and sea surface temperature in the Southern Hemisphere midlatitudes: A statistical assessment. *J. Climate*, **31**, 4055–4074, https://doi.org/10.1175/JCLI-D-17-0196.1.